

Metal-enriched Galaxies in the First ~ 1 Billion Years: Evidence of a Smooth Metallicity Evolution at $z \sim 5$

Suraj Poudel,^{1*} Varsha P. Kulkarni,¹ Frances H. Cashman,¹ Brenda Frye,²
Céline Péroux,^{3,4} Hadi Rahmani,^{4,5} and Samuel Quiret⁴

¹University of South Carolina, Dept. of Physics and Astronomy, Columbia, SC 29208, USA

²University of Arizona, Dept. of Astronomy and Steward Observatory, Tucson, AZ 85721, USA

³European Southern Observatory, Karl-Schwarzschild-Strasse 2, 85748 Garching bei Munchen, Germany

⁴Laboratoire d'Astrophysique de Marseille, UMR 7326, F-13388, Marseille, France

⁵Observatoire de Paris, 61 Avenue de l'Observatoire, 75014 Paris, France

Accepted XXX. Received YYY; in original form ZZZ

ABSTRACT

We present seven new abundance measurements of the elements O, C and Si at $z > 4.5$, doubling the existing sample of weakly depleted elements in gas-rich galaxies, in order to constrain the first ~ 1 billion years of cosmic metal evolution. These measurements are based on quasar spectra of damped Lyman-alpha absorbers (DLAs) and sub-DLAs obtained with the Magellan Inamori Kyocera Echelle (MIKE) and Magellan Echellette (MagE) spectrographs on Magellan-South, and the X-Shooter spectrograph on the Very Large Telescope. We combine these new measurements with those drawn from the literature to estimate the N_{HI} -weighted binned mean metallicity of -1.51 ± 0.18 at $z = 4.8$. This metallicity value is in excellent agreement with the prediction from lower redshift DLAs, supporting the interpretation that the metallicity evolution is smooth at $z \sim 5$, rather than showing a sudden decline at $z > 4.7$. Furthermore, the metallicity evolution trends for the DLAs and sub-DLAs are similar within our uncertainties. We also find that the [C/O] ratios for $z \sim 5$ DLAs are consistent with those of the very metal-poor DLAs. Additionally, using [C/O] and [Si/O] to constrain the nucleosynthesis models, we estimate that the probability distributions of the progenitor star masses for three relatively metal-poor DLAs are centered around $12 M_{\odot}$ to $17 M_{\odot}$. Finally, the $z \sim 5$ absorbers show a different metallicity-velocity dispersion relation than lower redshift DLAs, suggesting that they may be tracing a different population of galaxies.

Key words: ISM: abundances – galaxies: high-redshift – quasars: absorption lines

1 INTRODUCTION

Metal abundance measurements throughout the cosmic ages track the history of galaxy formation and evolution from the initial pristine stars and galaxies to the present day metal-rich galaxies. At $z \sim 5$, the cosmic stellar mass density is expected to have doubled every 300 Myr (e.g. Gonzalez et al. 2011). As a result, due to the finite age of the universe, metals observed in absorption at this epoch are only a few hundred million years old and are produced either by core-collapse supernovae of the massive metal-poor stars or by pair-instability supernovae. Therefore, the first 1 billion years of the cosmic metal evolution are influenced by the nucleosynthetic signatures from the early stars, and

measuring abundances during the $z \sim 5$ epoch can constrain the nature of the pristine Population III stars and the metal-poor Population II stars. The initial mass function of Population III stars is still a subject of debate, some studies suggest masses as high as $100 M_{\odot}$ (e.g. Bromm, Coppi & Larson et al. 1999; Nakamura & Umemura 2001; Abel et al. 2002), where other studies suggest somewhat smaller values. For example, fragmentation due to turbulence can result in smaller Population III IMF (Initial Mass Function) (Clark et al. 2011), and multiple smaller Population III stars can be formed in a given minihalo (e.g. Stacy & Bromm 2013; Hirano et al. 2014; Stacy et al. 2016). Measurements of relative abundances such as [C/O] in chemically young systems can put a strong constraint on the mass of the progenitor Population III stars (Cooke et al. 2017). Finally, abundance measurements can be compared with the results from different cosmic metal evolution models with the

* E-mail: spoudel@email.sc.edu

inclusion or exclusion of the Population III stars (e.g. [Maio & Teschari 2015](#); [Kulkarni et al. 2013](#)) to explore the early enrichment history of star formation and enrichment in galaxies.

While probing the chemical enrichment of galaxies from continuum or line emission is difficult at higher redshift, measurement of absorption lines in the spectra of background objects such as quasars provides a powerful method to measure chemical abundances (e.g. [Pettini et al. 1994](#); [Prochaska et al. 2003a](#); [Kulkarni et al. 2005](#)). Also, unlike emission-based detection, the absorption-based method can select gas-rich galaxies independent of their brightness ([Wolfe et al. 2005](#)). Particularly interesting absorption systems are the DLAs (Damped Lyman-alpha Absorbers) and sub-DLAs (sub-Damped Lyman-alpha Absorbers) in background quasar spectra, which have high neutral hydrogen column densities ($\log N_{\text{HI}} \geq 20.3$ and $19.0 \leq \log N_{\text{HI}} < 20.3$, respectively). DLAs and sub-DLAs together dominate the neutral gas mass density of the universe at high redshift (e.g. [Wolfe et al. 2005](#); [Zafar et al. 2013](#); [Berg et al. 2019](#)), and provide the neutral gas reservoir for star formation (e.g. [Nagamine et al. 2004a,b](#); [Wolfe & Chen. 2006](#)). The presence of damping wings in the Lyman-alpha lines for DLAs and sub-DLAs allows precise measurements of neutral hydrogen column densities. Furthermore, DLAs and sub-DLAs are also powerful probes of metals in the interstellar medium and the circumgalactic medium of distant galaxies. Finally, unlike the Lyman alpha forest and Lyman limit systems, DLAs are primarily neutral and insensitive to the ionization corrections (e.g. [Erb et al. 2006](#); [Aguirre et al. 2008](#); [Lehner et al. 2013](#)). From a number of previous observations, DLA metallicity is observed to decrease gradually from redshift $z = 0$ to $z = 4$ with a rate of about 0.2 dex per redshift (e.g. [Kulkarni & Fall 2002](#); [Prochaska et al. 2003a](#); [Kulkarni et al. 2005, 2007](#); [Rafelski et al. 2012](#); [Jorgenson et al. 2013](#); [Som et al. 2013, 2015](#); [Quiret et al. 2016](#)). However, the DLA metallicity evolution at high redshift is still unclear, primarily due to inadequate samples having robust measurements of dust-free metallicity. Some previous studies (e.g. [Rafelski et al. 2012, 2014](#)) reported a sudden decline of DLA metallicity at $z > 4.7$, suggesting a sudden change in the chemical enrichment process. However, such a sudden drop would be expected to be associated with a sudden change in the star formation history of galaxies, which is not observed. Indeed, the observed star formation history of galaxies based on UV and IR observations, shows no sudden change at $4 \lesssim z \lesssim 8$ ([Madau & Dickinson 2014](#)). Recent studies (e.g. [Morrison et al. 2016](#); [De Cia et al. 2018](#); [Poudel et al. 2018](#)) have shown that the sudden drop reported at $z > 4.7$ can be explained in terms of dust depletion, which cannot be ignored even at $z \sim 5$. As observed in the Milky Way (MW) Interstellar Medium (ISM), elements with a higher condensation temperature (e.g. Si, Fe etc) are subject to more depletion into dust grains than elements with a relatively lower condensation temperature (S, O, Zn etc). Even in DLAs the depletion is more severe for refractory elements like Si, Fe, than for volatile elements O, S (e.g. [De Cia et al. 2016](#)).

The results from a small sample of seven systems

[Poudel et al. \(2018\)](#) with dust-free abundance measurements suggests that the N_{HI} -weighted mean metallicity at $z \sim 5$ absorbers agrees with the prediction from $z < 4.5$ DLAs within $< 0.5\sigma$. Furthermore, the N_{HI} -weighted mean metallicity at $z \sim 5$ from [Poudel et al. \(2018\)](#) is in excellent agreement with results of recent simulations from [Finlator et al. \(2018\)](#).

Evolution of metallicity as a function of redshift is a powerful tracer of the cosmic star formation history. It is therefore important to determine the metallicity evolution of DLAs/sub-DLAs accurately. Given the potentially interesting implications of a sudden drop in metallicity at $z \sim 5$ and the conflict such a drop would produce with existing chemical evolution models, it is especially important to check with a larger sample whether or not such a sudden drop in metallicity actually exists. With this goal, we have been expanding measurements of S and/or O in other DLAs at $z \geq 4.5$. Here we present results of VLT and Magellan observations of 7 more absorbers in this redshift range. Inclusion of these new measurements doubles the current high- z sample of volatile elements, and thus offers a better understanding of DLA metallicity evolution at $z \sim 5$. We also examine the relative element abundances and their variation with velocity of the absorbing gas.

This paper is organized as follows: section 2 presents our observations and details of data reduction. Section 3 presents the measurements of the metal lines and determination of the element abundances. Section 4 describes the results for the individual absorbers. Section 5 presents a discussion of our results. Finally, section 6 summarizes our conclusions.

2 OBSERVATIONS AND DATA REDUCTION

Our sample consists of seven absorbers with neutral hydrogen column density of $\log N_{\text{HI}} = 19.65$ to 20.75, at redshifts 4.59 to 5.05 along the sight lines to four quasars. These absorbers were chosen from the $z > 4.5$ SDSS (Sloan Digital Sky Survey) absorbers with $\log N_{\text{HI}} \geq 20.0$ listed in [Noterdaeme et al. \(2012\)](#). To check the validity of the systems, the SDSS spectra were checked to make sure that at least 1 metal line of any low ion (e.g. C II, Si II, O I) was detected at the same redshift as the H I DLA redshift listed in [Noterdaeme et al. \(2012\)](#) (or within $\pm 1500 \text{ km s}^{-1}$ of that redshift), regardless of the strength of that metal line. In other words, the selection of the absorbers was driven by the redshift, the H I column density, and the mere existence of at least 1 other low-ionization metal line, but was independent of the strength of the metal line.

Two of the quasars J1557+1018 and J1253+1046 probing three absorbers were observed with MIKE in April 2017 on the Magellan Clay telescope at Las Campanas observatory in Chile (PI: Frye, 2017A). Observations were carried out with a 1" slit, and reached a spectral resolution of $\sim 22,000$ with the red arm and $\sim 28,000$ with the blue arm, giving a combined wavelength coverage of 3500 to 9400 Å. The quasar J1233+0622 was observed with X-Shooter in 2014, a medium resolution spectrograph on VLT (Very Large Telescope) with a spectral coverage of 3000 to 25,000

Å. While the near infrared arm of X-Shooter provides resolution of 5300, the visible arm of the spectrograph in which most of our lines fall, provides a resolution of 8900 with a 0.9" slit. Finally, J0306+1853 was observed with Magellan Echellette (MagE) in January 2014 using a 1" slit with a resolution of ~ 4100 over 6000-10,000 Å. The details of the observations are summarized in Table 1.

The MIKE data were reduced using the MIKE pipeline reduction code written in IDL and developed by S. Burles, J. X. Prochaska and R. Bernstein. The reduction package performs all the necessary steps for bias subtraction, flat fielding and sky-subtraction. Before and after each science exposure, comparison exposures using the Th-Ar lamp were taken for wavelength calibration purposes. After the calibration and the heliocentric velocity corrections, the pipeline extracts each individual echelle order from all the exposures. Multiple exposures were obtained and combined to facilitate the rejection of cosmic rays.

X-Shooter observations of J1233+0622 were reduced using the X-Shooter Common Pipeline Library (Goldoni et al. 2006) release 6.5.1¹ to obtain the flat fielded, wavelength calibrated and sky-subtracted 2D spectra from the 2-D raw images. The final 1-D spectrum was extracted using spectral point spread function (SPSF) subtraction as described in Rahmani (2016). The details of the reduction procedure are described in Poudel et al. (2018).

The MagE data were reduced using a custom-built pipeline and flux-calibrated using techniques described in Becker et al. (2015).

For all objects, the final 1-D spectra were continuum-normalized and multiple exposures were combined thereafter using IRAF².

3 VOIGT PROFILE FITTING AND ABUNDANCE MEASUREMENTS

We used the Voigt profile fitting program, VPFIT³ v. 10.0 for the determination of column densities of metal lines and neutral hydrogen. VPFIT minimizes the χ^2 residual between the data and theoretical Voigt profiles convolved with the instrumental line spread profile through multiple iterations. VPFIT makes it possible to perform simultaneous multi-component Voigt profile fitting of multiple lines of multiple ions, while allowing the Doppler b parameters and redshifts of the corresponding components to be tied together. While the line blending can be an issue with lower resolution spectrographs, three out of the seven absorbers in our sample have a relatively higher resolution of 13.7 km s^{-1} which can resolve the blending of metal lines. For many of the systems we were also

able to use multiple lines to minimize the error caused by possible saturation effects (e.g. Penprase et al. 2010). The fitted column densities and associated uncertainties determined with VPFIT were confirmed by comparing the calculated and observed line profiles (in the core as well as the wings) and verifying that the profiles agreed within the noise level present. Another potential issue with high-redshift systems is the severe blending of metal lines with hydrogen lines in the dense Lyman forest. However, all of the lines used for the column density determinations were outside the Lyman-alpha forest and were not affected by the forest lines. For the sake of comparison, we have also included apparent optical depth (AOD) column densities (e.g. Savage & Sembach 1991) in addition to the column densities derived from the Voigt profile fitting for all of our systems. In most cases, the column densities estimated from the AOD method are consistent with those estimated from the Voigt profile fitting method within $\sim 1\sigma$. In cases with only one saturated line each for O I and/or C II, the AOD method cannot give reliable lower limits to the column densities. Limits from a linear curve of growth are also not applicable for such saturated lines. In such cases, we adopt the lower limits obtained from Voigt profile fitting.

Another challenge affecting high-redshift systems is the continuum normalization blueward of the Lyman-alpha emission. This is partly due to severe blending with the Lyman-alpha forest and partly because of the relatively low signal-to-noise ratio for the faint quasars. The typical resolution of $13 - 55 \text{ km s}^{-1}$ used for most of our absorbers, was adequate to resolve the forest for determining the neutral hydrogen column density. For each sightline, we selected the entire available spectrum blueward of the Lyman-alpha emission for the continuum normalization. In most cases, the spectra covered at least the first three Lyman-series lines. Regions of the spectra unaffected by any absorption were selected to fit the continuum. A spline polynomial, typically of order 5, was fitted to the selected continuum region using the CONTINUUM task in IRAF. H I column densities were estimated by fitting Voigt profiles to the Lyman series lines that were usable. For most of the systems, the H I column densities were measured by fitting Voigt profiles to the Lyman-alpha lines taking the core and the wings of the profiles into consideration (e.g. Poudel et al. 2018). In some cases, we were able to use both the Lyman-beta and the Lyman-alpha lines to estimate the H I column densities. While the Lyman-alpha lines for the absorbers at $z=4.589, 4.600$ along the sightline to the quasar J1253+1046 were blended with each other, we were able to make a joint fit of Lyman-alpha and Lyman-beta lines of these two systems together to estimate the H I column densities for both the absorbers. Moreover, both the Lyman-alpha and Lyman-beta lines were used to estimate the H I column density for the absorber at $z=4.987$ towards J0306+1853. In several cases, Lyman-series lines beyond Lyman-alpha were not useful, partly due to severe blending with the dense Lyman-alpha forest at these high redshifts, and partly due to the high noise level (see Fig. B1 and Fig. B2 in Appendix B). To estimate the uncertainties in the H I column densities, we examined the range of values for which the fitted profiles are consistent with the observed data within the noise level (e.g. Poudel et al. 2018). We note that

¹ <http://www.eso.org/sci/facilities/paranal/instruments/xshooter/>

² IRAF is distributed by the National Optical Astronomy Observatory, which is operated by the Association of Universities for Research in Astronomy, Inc., under cooperative agreement with the National Science Foundation.

³ <https://www.ast.cam.ac.uk/rfc/vpfit.html>

the uncertainties thus estimated are more conservative than estimates based on the continuum placement errors alone. (The uncertainties in the H I column densities contributed by error in continuum placement were estimated by shifting the continuum up and down by the 1σ uncertainty, renormalizing the continuum at those levels, and then refitting the Voigt profiles in each case. The uncertainties in the H I column densities resulting from continuum placement errors thus derived were typically $\lesssim 0.1$ dex)

We have not made ionization corrections to any of the abundances since observations of higher ionization lines are not available to place constraints on the ionization parameter. In any case, the ionization corrections are expected to be negligible for DLAs and $\lesssim 0.2$ dex for sub-DLAs (e.g. Dessauges-Zavadsky et al. 2003; Meiring et al. 2009; Cooke et al. 2011; Som et al. 2015).

All abundances reported in this paper are relative to the solar abundances taken from Asplund et al. (2009). The rest-frame wavelengths and oscillator strengths used for the Voigt profile fitting were taken from Morton (2004) and Cashman et al. (2017).

4 RESULTS FOR INDIVIDUAL ABSORBERS

In this section, we report the results for the column densities derived from Voigt profile fitting, the inferred absolute and relative abundances, and the gas kinematics determined from velocity dispersion measurements for individual absorbers. For each system, the H I lines are shown in Fig. 1.

4.1 Absorber at $z = 4.987$ along the sight line to J0306+1853

This absorber was observed with lower spectral resolution than the other absorbers and was initially reported in Wang et al. (2015). We reanalyzed this system by doing Voigt profile fitting for O I $\lambda 1302$, Si II $\lambda 1304$, and C II $\lambda 1334$ and calculated the corresponding element abundances. Fig. 2 shows the Voigt profile fits for the metal lines. This system is a metal-poor DLA with $\log N_{\text{HI}} = 20.60 \pm 0.15$ and $[\text{O}/\text{H}] = -2.69 \pm 0.17$. Our estimate of N_{HI} is consistent with the estimate $\log N_{\text{HI}} = 20.50^{+0.10}_{-0.12}$ of Wang et al. (2015). Wang et al. (2015) had estimated $\log N_{\text{SiII}} = 14.8$ using the apparent optical method for Si II $\lambda 1304$ and Si II $\lambda 1527$, and thereby estimated $[\text{Si}/\text{H}] = -1.3 \pm 0.1$. The Si II $\lambda 1527$ line is, however, blended significantly. We therefore did Voigt profile fitting for only the Si II $\lambda 1304$ line and got a lower Si II column density $\log N_{\text{SiII}} = 14.22$. The apparent optical depth method applied to this line also gives a similar value for the Si II column density.

By comparison, the O I $\lambda 1302$ line is weak, implying that Si is strongly enhanced relative to O, with $[\text{Si}/\text{O}] = 0.79 \pm 0.09$. Such a high $[\text{Si}/\text{O}]$ value is surprising, given that Si and O are both alpha-elements. Thus, $[\text{Si}/\text{O}]$ or $[\text{Si}/\text{S}]$ is usually either zero (in the absence of dust depletion) or negative (in the presence of dust depletion, since Si is more severely depleted than the more volatile elements O or S). Given the relative weakness of O I $\lambda 1302$, the high $[\text{Si}/\text{O}]$

value is not expected to be an artifact of saturation. Nevertheless, higher resolution observations of this sight line would help to determine the column densities more accurately.

4.2 Absorber at $z = 4.859$ along the sight line to J1233+0622

A DLA at $z = 4.859$ along the sight line to J1233+0622 has been detected with $\log N_{\text{HI}} = 20.75 \pm 0.15$. The Voigt profile fits for the metal lines are shown in Fig. 3. While C II $\lambda 1334$, Fe II $\lambda 2600$, and Si II $\lambda 1527$ are detected for this system, the high- and low-velocity components for the O I $\lambda 1302$ line are blended with telluric absorption. This absorber is spread over a large radial velocity range with at least seven components detected in C II $\lambda 1334$ with X-Shooter resolution. This absorber shows some variations among different velocity components. For example, three of the components seen in Si II $\lambda 1527$ do not seem to be perfectly matched with those in C II $\lambda 1334$. We believe there is no possibility of blending in Si II $\lambda 1527$, since it lies outside the Lyman-alpha forest, and the only other known absorber in this sightline does not have suitable lines that could cause blending. We also do not find any obvious problems with data reduction. The differences between the Si II $\lambda 1527$ and C II $\lambda 1334$ lines may thus arise partly due to a slight offset in the wavelength calibrations of the visible and near-IR parts of X-Shooter spectra and partly from the differences in ionization, depletion, or intrinsic nucleosynthetic ratios. Such differences in nucleosynthesis/depletion have been reported before in other high-redshift absorbers even with the higher spectral resolution of Keck HIRES (e.g. Morrison et al. 2016). Moreover, we are able to estimate the lower limit of the O I $\lambda 1302$ column density by overfitting the profile for the central main component, fixing the redshift and Doppler b parameter determined in C II $\lambda 1334$. Taking only this central component (excluding the other components that are heavily blended with telluric absorption features), we place a lower limit on $[\text{O}/\text{H}] > -2.14$. For C II $\lambda 1334$, as shown in Fig. A1, we have analyzed the effect of changing the column density for the strongest component in steps of 0.1 dex. The difference between the profile and the data becomes large, considering the 1σ uncertainty in the normalized flux, if the C II column density is increased by > 0.1 dex compared to the adopted value of 14.42. This is consistent with the uncertainty of 0.07 dex obtained from VPFIT. The Fe II profile seems to differ in structure from C II and Si II profiles in the sense that almost no Fe II is seen in the central components seen in C II and Si II. The peak Fe II absorption seems to be blue-shifted by $\sim 50 \text{ km s}^{-1}$ with respect to the peak absorption in C II and Si II.

4.3 Absorber at $z = 5.050$ along the sight line to J1233+0622

The quasar sight line to J1233+0622 shows a second absorber at $z = 5.050$ with $\log N_{\text{HI}} = 20.10 \pm 0.15$. This absorber is detected in O I $\lambda 1302$, C II $\lambda 1334$, Si II $\lambda 1304$, Si II $\lambda 1527$, and Fe II $\lambda 1608$. The corresponding Voigt profile fits are shown in Fig. 4. This is also a metal-rich absorber which shows multiple components spread over a large radial

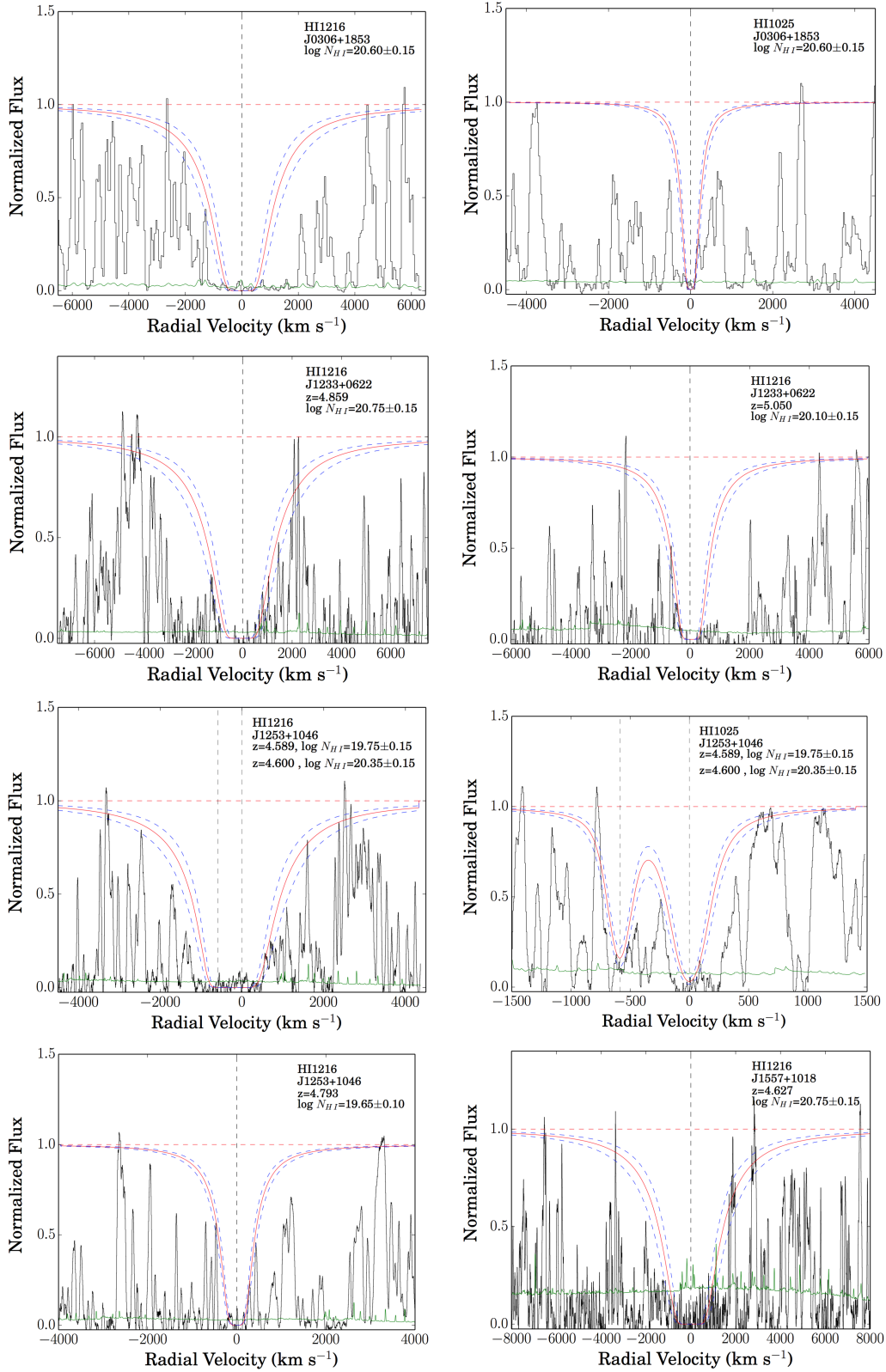


Figure 1. Plots showing the estimation of neutral hydrogen column densities for all of the absorbers. In each case, the observed continuum normalized flux is shown in black and the best fitted profile is shown in red. The blue dashed curves above and below the fitted profile represent the uncertainty in the column density determination. The 1σ error in the normalized flux is shown in green at the bottom of each panel. The centre of the profile is fixed at the redshift determined during metal line fitting and is shown as a black dashed line. The placement of continuum is shown by the horizontal dashed red line. Lyman-alpha and Lyman-beta were used to determine hydrogen column density for an absorber at $z=4.987$ toward J0306+1853 and the two absorbers at $z=4.589$, 4.600 toward J1253+1046, while only Lyman-alpha was used for the other absorbers (see text for further details). The estimated $\log N_{\text{HI}}$ values and redshifts are mentioned in the top right corner of each panel.

Table 1. Summary of targets and observations

QSO RA(J2000), Dec(J2000)	m_i	z_{em}	z_{abs}	$\log N_{\text{HI}}$	Instrument	Exposure Time (s)	Wavelength Coverage(Å)	Spectral Resolution (R)
J0306+1853 RA: 03:06:42.51; Dec: +18:53:15.8	17.96	5.363	4.987	20.60±0.15	Magellan MagE	1800 × 3	6000-10,000	4100
J1233+0622 RA: 12:33:33.47; Dec: +06:22:34.3	20.09	5.311	4.859 5.050	20.75±0.15 20.10±0.15	VLT X-Shooter	3600	3000-25,000	VIS: 8800 NIR: 5300
J1253+1046 RA: 12:53:53.35; Dec: +10:46:03.1	19.40	4.925	4.589 4.600 4.793	19.75±0.15 20.35±0.15 19.65±0.10	Magellan MIKE	2700 × 3	3500-9,400	Red: 22,000 Blue: 28,000
J1557+1018 RA: 15:57:00.17; Dec: +10:18:41.8	19.98	4.765	4.627	20.75±0.15	Magellan MIKE	2700 × 5	3500-9,400	Red: 22,000 Blue: 28,000

velocity range with $[\text{O}/\text{H}]$ of -1.60 ± 0.18 . Furthermore, we have analyzed the effect of changing the column density for the strongest component both in O I $\lambda 1302$ and C II $\lambda 1334$ in steps of 0.1 dex (see Fig. A1). The difference between the data and the profile becomes large, considering the 1σ uncertainty in the normalized flux, if the column density is increased by >0.1 dex for O I and >0.2 dex for C II compared to the adopted column density values. Thus the uncertainties in the column densities are consistent with the values obtained from VPFIT (0.12 dex for O I and 0.16 dex for C II). As Si II $\lambda 1527$ is saturated, we used Si II $\lambda 1304$ to estimate the abundance for silicon. While oxygen and carbon are detected in multiple components, the absence of some corresponding components in silicon might suggest spatial variation in the dust depletion. The central velocity of the Fe II profile is consistent with the velocities of the main components in O I, C II and Si II profiles.

4.4 Absorber at $z = 4.589$ along the sight line to J1253+1046

The sight line to quasar J1253+1046 probes a sub-DLA at a redshift $z = 4.589$. Although the Lyman-alpha for this absorber is heavily blended with a nearby absorber, making it difficult to determine the hydrogen column density, we were able to use the less blended Lyman-beta line, and estimate $\log N_{\text{HI}} = 19.75 \pm 0.15$. The corresponding Voigt profile fits for O I $\lambda 1302$, C II $\lambda 1334$, Si II $\lambda 1527$, and Fe II $\lambda 1608$ are shown in Fig. 5. O I $\lambda 1302$ is saturated, but based on Fig. A1, the O I column density for the strongest component cannot be higher by > 0.2 dex than the adopted value due to the effect in the line wings. Also, the difference between the data and the profile for C II $\lambda 1334$ becomes large if the column density is increased by >0.2 dex compared to the adopted value, which is consistent with the uncertainty of 0.22 dex obtained from VPFIT. The $[\text{O}/\text{H}]$ value of -1.43 ± 0.17 for this absorber suggests this as a metal-rich sub-DLA. Besides the main component, oxygen is the only element showing multiple components, one at -40 km s^{-1} and another at 43 km s^{-1} . Oxygen seems to be enhanced over silicon suggesting possible depletion into dust grains. Surprisingly, one of

these higher velocity components seen in O I but not in C II or Si II is seen in Fe II. Furthermore, as in the case of the $z = 4.859$ absorber toward J1233+0622, the main central component seen in O I, C II, and Si II is not seen in Fe II. The center of the Fe II profile seems to be blue-shifted by $\sim 35 \text{ km s}^{-1}$ with respect to the central components in O I, C II, and Si II.

4.5 Absorber at $z = 4.600$ along the sight line to J1253+1046

The quasar sight line to J1253+1046 also shows a DLA absorber at $z = 4.600$. The column density estimation for Lyman-alpha gives $\log N_{\text{HI}} = 20.35 \pm 0.15$. O I $\lambda 1302$, C II $\lambda 1334$, Si II $\lambda 1304$, Si II $\lambda 1527$, and Fe II $\lambda 1608$ are detected in this absorber and the corresponding Voigt profile fits are shown in Fig. 6. This is a metal-rich DLA, $[\text{O}/\text{H}]$ has a lower limit of -1.46 . Since C II $\lambda 1334$ is also saturated, we adopted a lower limit as shown in Table. 3. This absorber also shows spatial variation in the relative abundances as two extra components are detected in O I $\lambda 1302$ but not in silicon and carbon. Once again, the Fe II profile is quite distinct from the profiles of O I, C II, Si II, and seems to be shifted to the blue by $\sim 50 \text{ km s}^{-1}$.

4.6 Absorber at $z = 4.793$ along the sight line to J1253+1046

This is the second sub-DLA detected along the same sight line to J1253+1046 with $\log N_{\text{HI}} = 19.65 \pm 0.10$. Besides O I $\lambda 1302.2$, C II $\lambda 1334.5$, Si II $\lambda 1304.4$, Si II $\lambda 1260.4$, Si II $\lambda 1527$, this absorber also shows detection of S II $\lambda 1254, 1260$. The corresponding Voigt profile fits are shown in Fig. 7. Since O I $\lambda 1302$ is saturated, the abundance based on Voigt profile fitting has a lower limit of -1.63 . However, the difference between the data and the profile for C II $\lambda 1334$ based on Fig. A1 becomes large if the C II column density is increased by >0.2 dex compared to the adopted value, which is consistent with the uncertainty of 0.17 dex obtained from VPFIT. Moreover, the sulphur abundance is significantly higher with a value of $[\text{S}/\text{H}] = -0.59 \pm 0.20$. In fact, such a

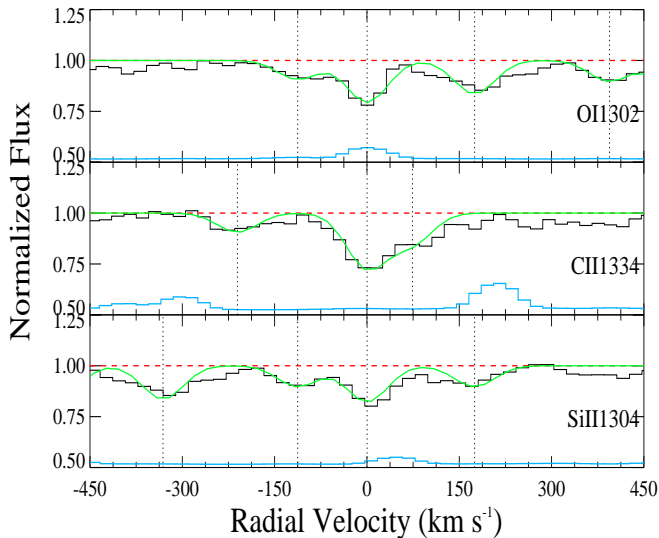


Figure 2. Velocity plots for metal lines for the absorber at $z = 4.987$ in the sight line to J0306+1853 from the MagE spectrograph. In each panel, the observed data are shown in black and the fitted profiles are shown in green. The blue line at the bottom of each panel shows the 1σ error in the normalized flux and is shifted by +0.5. The placement of continuum is shown by the horizontal dashed red line. The vertical dotted lines show the different velocity components included in the profile fits. It is to be noted that the rightmost vertical dotted line in O I $\lambda 1302$ is attributed to Si II absorption and the leftmost vertical dotted line in Si II $\lambda 1304$ is attributed to O I absorption.

high metallicity is quite rare in DLAs even at $z < 2$. Also, Si shows a much smaller abundance than S, suggesting strong dust depletion. To date, this absorber has the highest metallicity among $z > 4.5$ sub-DLAs or DLAs.

4.7 Absorber at $z = 4.627$ along the sight line to J1557+1018

The sight line to J1557+1018 shows a DLA at $z = 4.627$ that was estimated by [Noterdaeme et al. \(2012\)](#) to have $\log N_{\text{HI}} = 21.30$ based on its SDSS spectrum. Based on our higher resolution MIKE spectrum, we get a value of $\log N_{\text{HI}} = 20.75 \pm 0.15$. However, we note that the S/N at the position of the Lyman-alpha line is low. Higher S/N data would be useful to obtain a more definitive determination of N_{HI} in this absorber. Fig. 8 shows the fitted metal lines for O I $\lambda 1302$, C II $\lambda 1334$, Si II $\lambda 1304$, and Si II $\lambda 1527$.

All the accessible absorption lines in this absorber are saturated. Thus we can estimate only lower limits on the metal column densities and the corresponding element abundances. For example, based on O I $\lambda 1302$, we estimate $[\text{O}/\text{H}] \geq -1.47$. This DLA is thus remarkably metal-rich for its high redshift.

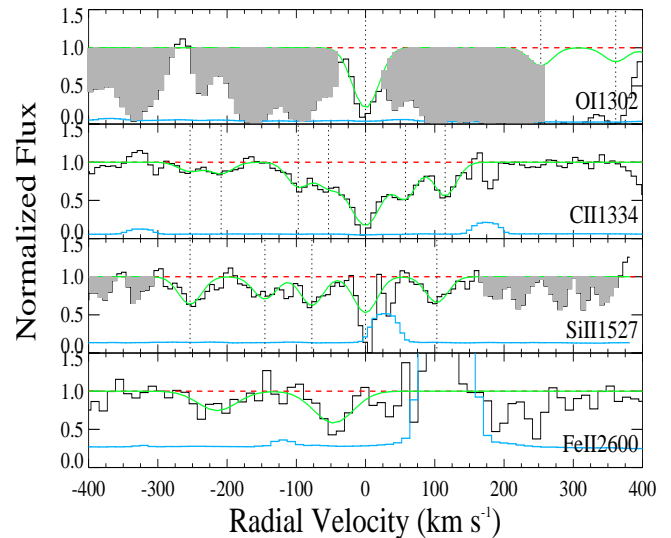


Figure 3. Velocity plots for metal lines for the absorber at $z = 4.859$ in the sight line to J1233+0622 from the X-Shooter spectrograph. In each panel, the observed data are shown in black and the fitted profiles are shown in green. The blue line at the bottom of each panel shows the 1σ error in the normalized flux and the placement of continuum is shown by the horizontal dashed red line. The vertical dotted lines show the different velocity components included in the profile fits. The shaded regions are the telluric and unrelated absorption features.

5 DISCUSSION

Now we combine our measurements with those from the literature and perform a comparative study of metallicity-velocity dispersion, relative abundances, dust depletion, and metallicity evolution.

5.1 Profile Shapes and the Metallicity vs. Velocity Dispersion Relation

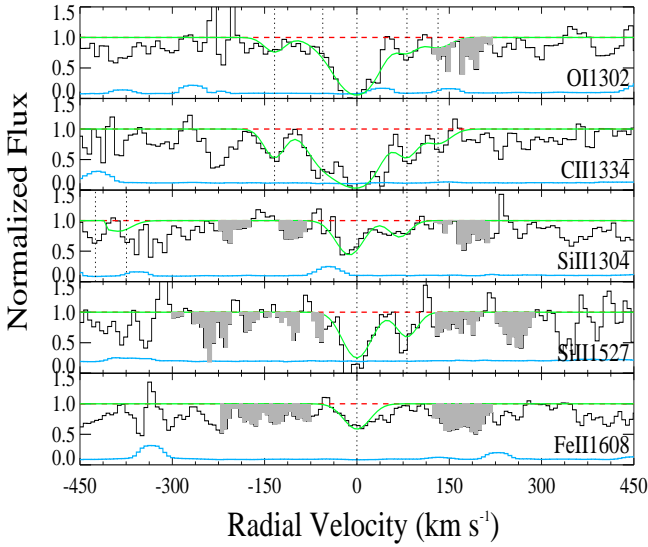
The gas kinematics of a galaxy can be understood from the measurement of velocity dispersion of its gas. One measure of the gas velocity dispersion is the quantity Δv_{90} , i.e., the velocity range that spans 90 percent of the total absorption determined from relatively weak and unsaturated metal lines whenever possible (e.g. [Wolfe & Prochaska 1998](#)). Fig. 9 shows the measurements of velocity dispersion for all the absorbers in this paper using weaker and unsaturated transitions where available. We treat the Δv_{90} derived from the strong, saturated lines as upper limits. To estimate Δv_{90} , we measure the radial velocity width between 5 percent and 95 percent of the integrated optical depth using the fitted profiles as shown in Fig. 9. The value of the velocity dispersion may depend on the inflow or outflow of gases within the galaxy and also on the mass of the galaxy. If the velocity dispersion depends primarily on mass, and the role played by gas flows is small, then the velocity dispersion vs.

Table 2. Results of Voigt profile fitting for different elements in the absorbers along the sight lines of all quasars in our sample. For the sake of comparison, the total AOD column densities for each of these systems are also given, where available, under the Voigt profile results.

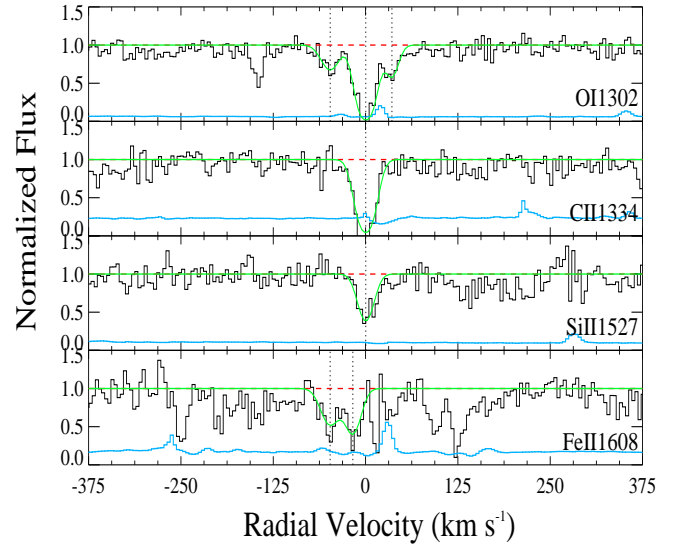
z	b_{eff} (km s ⁻¹)	log N_{OI}	log N_{CII}	log N_{SiII}	log N_{FeII}	log N_{SII}
J0306+1853, $z_{\text{abs}} = 4.987$						
4.98241 ± 0.00004	5.23 ± 7.14	...	13.40 ± 0.18
4.98436 ± 0.00001	4.54 ± 2.09	13.86 ± 0.12	...	13.68 ± 0.09
4.98661 ± 0.00004	8.54 ± 1.63	14.28 ± 0.16	14.13 ± 0.15	13.90 ± 0.07
4.98808 ± 0.00001	4.53 ± 7.14	...	13.88 ± 0.28
4.99010 ± 0.00002	7.44 ± 3.41	14.14 ± 0.06	...	13.58 ± 0.07
Total log N	...	14.60 ± 0.08	14.37 ± 0.13	14.22 ± 0.05
AOD log N	...	14.48 ± 0.03	14.12 ± 0.04	14.05 ± 0.04
J1233+0622, $z_{\text{abs}} = 4.859$						
4.85300 ± 0.00003	10.46 ± 2.83	...	13.09 ± 0.21	13.61 ± 0.21
4.85388 ± 0.00002	10.46 ± 4.11	...	13.19 ± 0.18	...	13.13 ± 0.20	...
4.85511 ± 0.00003	12.23 ± 4.19	13.48 ± 0.23
4.85644 ± 0.00005	8.25 ± 1.13	13.68 ± 0.24
4.85691 ± 0.00006	8.71 ± 2.34	...	13.61 ± 0.10	...	13.44 ± 0.16	...
4.85795 ± 0.00004	18.12 ± 4.14	> 15.30	14.42 ± 0.07	13.82 ± 0.19
4.85908 ± 0.00004	7.53 ± 2.04	...	14.01 ± 0.14
4.85996 ± 0.00005	8.46 ± 3.04	13.59 ± 0.24
4.86019 ± 0.00003	8.46 ± 2.44	...	13.89 ± 0.11
4.86605 ± 0.00006	8.25 ± 2.04	...	13.63 ± 0.11
Total log N	...	> 15.30	14.74 ± 0.05	14.35 ± 0.10	13.61 ± 0.13	...
AOD log N	14.65 ± 0.02	14.44 ± 1.16	13.68 ± 0.12	...
J1233+0622, $z_{\text{abs}} = 5.050$						
5.04754 ± 0.00015	10.11 ± 1.12	13.88 ± 0.18	13.89 ± 0.19
5.04912 ± 0.00002	24.66 ± 2.47	13.79 ± 0.28	14.05 ± 0.14
5.05024 ± 0.00001	30.17 ± 3.02	15.11 ± 0.12	14.75 ± 0.16	14.19 ± 0.11	14.07 ± 0.09	...
5.05188 ± 0.00004	10.71 ± 2.09	13.88 ± 0.19	13.84 ± 0.19	13.69 ± 0.17
5.05290 ± 0.00015	18.58 ± 1.89	13.76 ± 0.20	13.49 ± 0.23
Total log N	...	15.19 ± 0.10	14.93 ± 0.11	14.31 ± 0.09	14.07 ± 0.09	...
AOD log N	...	15.11 ± 0.41	14.80 ± 0.05	14.27 ± 0.05	14.14 ± 0.05	...
J1253+1046, $z_{\text{abs}} = 4.589$						
4.58859 ± 0.00001	13.94 ± 3.69	13.84 ± 0.08	13.98 ± 0.14	...
4.58916 ± 0.00005	11.44 ± 7.14	13.89 ± 0.17	...
4.58948 ± 0.00004	11.44 ± 4.73	14.94 ± 0.10	14.34 ± 0.22	13.67 ± 0.09
4.59014 ± 0.00003	8.38 ± 2.36	13.86 ± 0.07
Total log N	...	15.00 ± 0.08	14.34 ± 0.22	13.67 ± 0.09	14.24 ± 0.11	...
AOD log N	...	14.78 ± 0.27	14.29 ± 0.38	13.88 ± 0.04	14.28 ± 0.06	...
J1253+1046, $z_{\text{abs}} = 4.600$						
4.59845 ± 0.00002	32.33 ± 3.41	14.32 ± 0.12
4.59940 ± 0.00005	23.24 ± 7.14	14.06 ± 0.29	...
4.60003 ± 0.00003	30.37 ± 1.63	15.53 ± 0.08	14.78 ± 0.20	14.57 ± 0.05
4.60194 ± 0.00003	19.61 ± 2.09	14.32 ± 0.09
Total log N	...	> 15.58	> 14.78	14.57 ± 0.05	14.06 ± 0.29	...
AOD log N	...	15.31 ± 0.06	14.78 ± 0.45	14.56 ± 0.01	14.26 ± 0.05	...
J1253+1046, $z_{\text{abs}} = 4.793$						
4.79347 ± 0.00001	10.00 ± 1.24	> 14.71	14.21 ± 0.17	14.15 ± 0.18	...	14.18 ± 0.17
AOD log N	...	14.56 ± 0.12	14.22 ± 0.07	14.08 ± 0.07	...	14.25 ± 0.04
J1557+1018, $z_{\text{abs}} = 4.627$						
4.62512 ± 0.00004	10.76 ± 1.17	14.54 ± 0.11	14.38 ± 0.15	13.65 ± 0.06
4.62694 ± 0.00002	35.53 ± 3.75	15.64 ± 0.09	15.52 ± 0.11	15.00 ± 0.04
4.62885 ± 0.00003	38.41 ± 4.84	15.55 ± 0.19	15.10 ± 0.21	14.74 ± 0.04
4.63018 ± 0.00015	14.29 ± 3.43	15.01 ± 0.19	14.53 ± 0.19	14.35 ± 0.09
Total log N	...	> 15.97	> 15.71	> 15.26
AOD log N	...	15.64 ± 0.62	15.23 ± 0.11	15.26 ± 0.84

Table 3. Relative abundances and velocity dispersions

Relative abundances	J0306+1853 $z_{abs} = 4.987$	J1233+0622 $z_{abs} = 4.859$	J1233+0622 $z_{abs} = 5.050$	J1253+1046 $z_{abs} = 4.589$	J1253+1046 $z_{abs} = 4.600$	J1253+1046 $z_{abs} = 4.793$	J1557+1018 $z_{abs} = 4.627$
[O/H]	-2.69 ± 0.17	> -2.14	-1.60 ± 0.18	-1.43 ± 0.17	> -1.46	> -1.63	> -1.47
[C/H]	-2.66 ± 0.19	-2.44 ± 0.15	-1.60 ± 0.19	-1.84 ± 0.27	> -2.0	-1.87 ± 0.20	> -1.47
[Si/H]	-1.89 ± 0.16	-1.91 ± 0.18	-1.30 ± 0.18	-1.59 ± 0.17	-1.29 ± 0.16	-1.01 ± 0.21	> -1.00
[S/H]	-0.59 ± 0.20	...
[Fe/H]	...	-2.64 ± 0.20	-1.53 ± 0.17	-1.01 ± 0.18	-1.79 ± 0.33
[C/O]	0.03 ± 0.15	< -0.30	0.00 ± 0.15	-0.41 ± 0.24	...	< -0.24	...
[Si/O]	0.79 ± 0.09	< 0.23	0.30 ± 0.14	-0.16 ± 0.12	< 0.17	< 0.62	...
[Fe/O]	...	< -0.50	0.07 ± 0.14	0.42 ± 0.14	< -0.33
[Si/C]	0.76 ± 0.13
Velocity dispersion	328.4 km s^{-1}	$< 322.3 \text{ km s}^{-1}$	114.0 km s^{-1}	25.4 km s^{-1}	88.3 km s^{-1}	21.0 km s^{-1}	$< 209.3 \text{ km s}^{-1}$


Figure 4. Same as Fig. 3 but for the absorber at $z = 5.050$ in the sight line to J1233+0622. Unrelated absorption features are shaded in grey.

metallicity relation can suggest a relationship between mass and metallicity (MZR) of absorber host galaxies. In lower redshift DLAs and sub-DLAs, a fairly tight correlation exists between the metallicity and the velocity dispersion of the gas (e.g. Péroux et al. 2003; Ledoux et al. 2006; Moller et al. 2013; Som et al. 2015). However, this relation is still unknown for high- z absorbers. Based on a small sample, Poudel et al. (2018) reported a somewhat flatter relation at $z \sim 5$. Fig. 10 shows the metallicity vs. velocity dispersion relation for the absorbers presented in this paper, along with those from Poudel et al. (2018) and other sources from the literature. This larger sample also shows a much


Figure 5. Velocity plots for metal lines for the absorber at $z = 4.589$ in the sight line to J1253+1046 from the MIKE spectrograph. In each panel, the observed data are shown in black and the fitted profiles are shown in green. The blue line at the bottom of each panel shows the 1σ error in the normalized flux and the placement of continuum is shown by the horizontal dashed red line. The vertical dotted lines show the different velocity components included in the profile fits.

flatter metallicity vs. velocity dispersion relation at $z > 4.5$ than for the $z < 4.5$ absorbers. Since we don't find the well established metallicity vs. velocity dispersion trend seen at lower redshifts, it is possible that the strength of the correlation decreases with increasing redshift.

A flatter metallicity vs. velocity dispersion relation could be caused by stronger inflows of metal-poor gas at

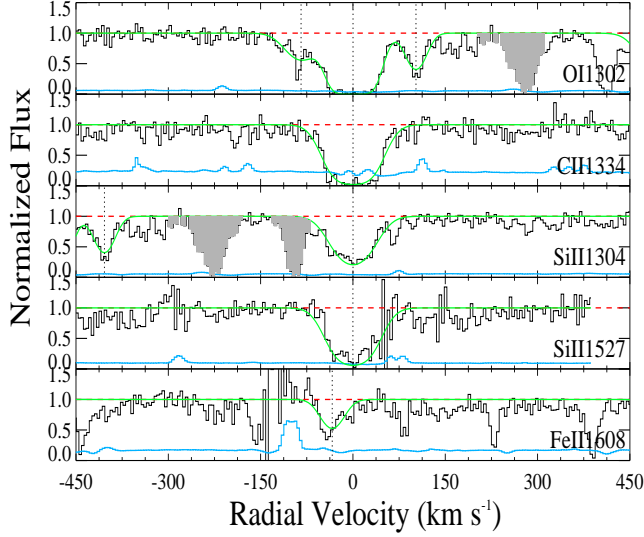


Figure 6. Same as Fig. 5 but for the absorber at $z = 4.600$ in the sight line to J1253+1046. The shaded regions are unrelated absorption features.

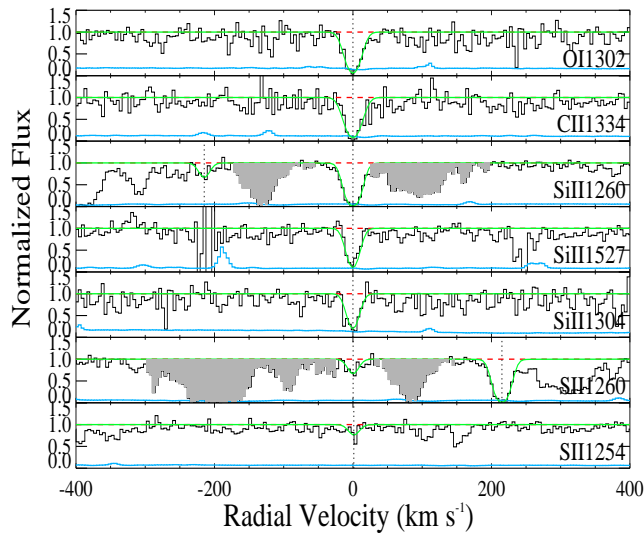


Figure 7. Same as Fig. 5 but for the absorber at $z = 4.793$ in the sight line to J1253+1046. The shaded regions are unrelated absorption features.

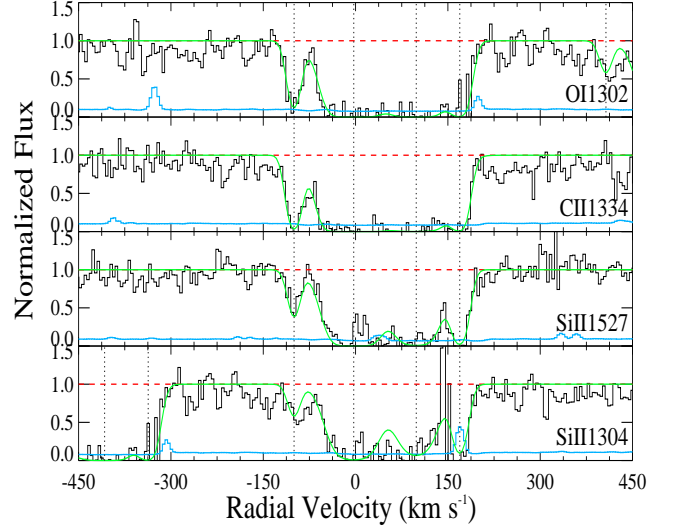


Figure 8. Same as Fig. 5 but for the absorber at $z = 4.627$ in the sight line to J1557+1018.

$z > 4.5$. Alternatively, if the velocity dispersion is dependent of the galaxy mass, then we speculate that the flatter trend for $z > 4.5$ absorbers may suggest that these absorbers are more dominated by dark matter and thus have lower stellar mass and lower metallicity.

Finally, we note that the velocity profile shapes show some potentially interesting differences. For example, for 3 of the 4 absorbers where we have measurements of Fe II profiles, we see a blueshift in the Fe II profiles with respect to the O I, C II, and Si II profiles. These 3 absorbers are at $z = 4.59$, 4.60 , and 4.86 . Such a shift, if real, would be unusual, compared to lower-redshift DLAs, even the VMP DLAs in Cooke et al. (2017). However, we note that not all of our high- z absorbers show a blueshift in the Fe II profile. For example, such a shift is not seen in the $z = 5.05$ absorber toward J1233+0622, or in either of the 2 absorbers in Poudel et al. (2018) at $z = 4.81$ or $z = 4.83$ where Fe II was observed. While for the $z = 4.86$ absorber toward J1233+0622, the shift in the Fe II absorption could arise partly due to a slight offset in the wavelength calibrations of the visible and near-IR parts of the X-Shooter spectra, we do not find any offsets in the wavelength calibration of the MIKE data for the absorbers at $z = 4.59$, 4.60 toward J1253+1046. For the absorbers presented here that do show a shift in Fe II profiles, the shift could be indicative of moderate-velocity outflows enriched in Fe II by type Ia supernovae. Alternately, the Fe II profiles may seem shifted if the central components arise in systematically more dusty regions leading to stronger depletion of Fe II in those components. However, the possibility of systematic dust depletion occurring in each case is small. Observations of more high- z DLA/sub-DLAs

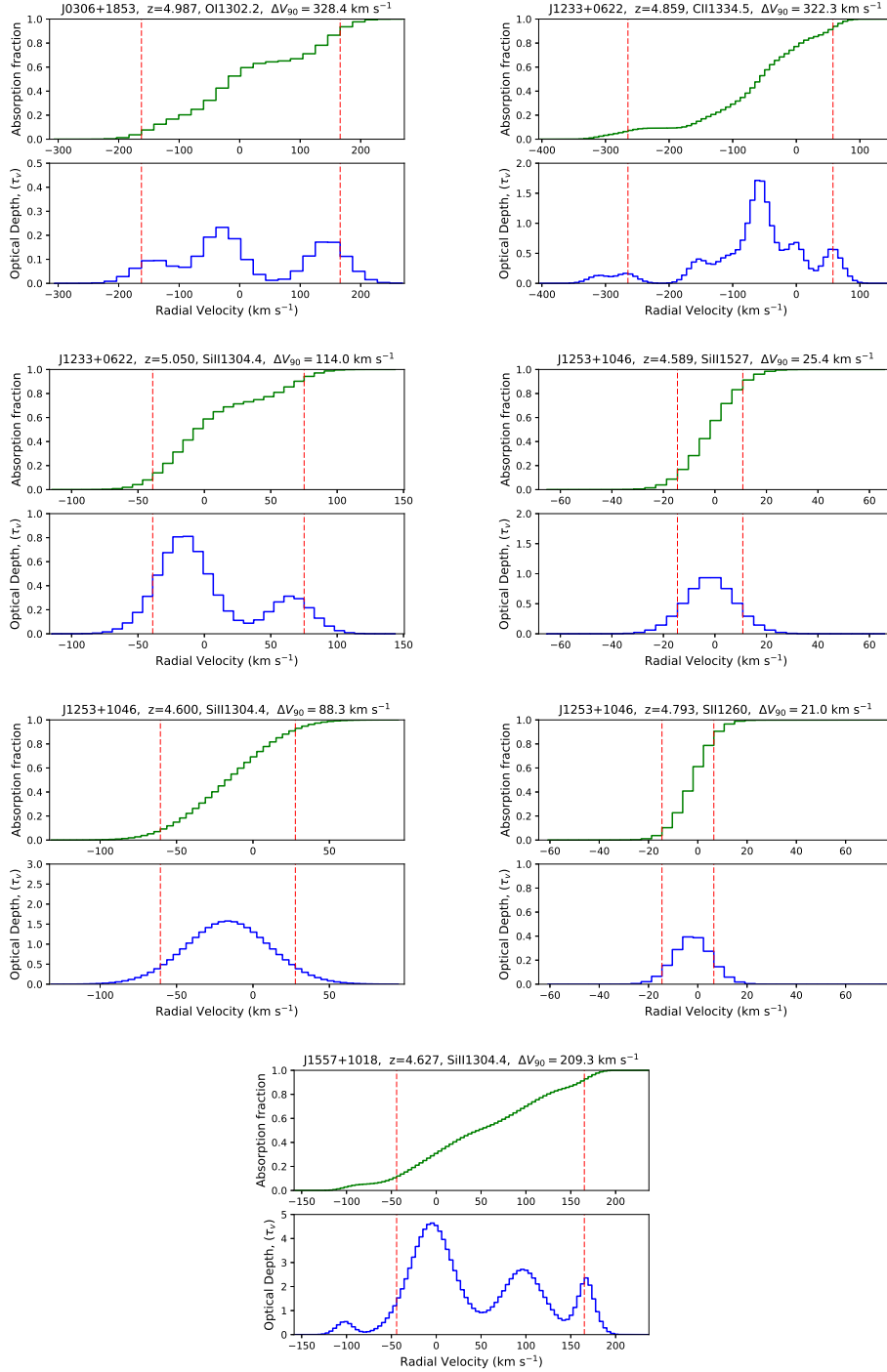


Figure 9. Plots showing absorption fraction vs. radial velocity (upper panel) and optical depth vs. radial velocity (lower panel) for metal lines from this work. The names of the sight lines, redshifts of the absorbers, names of the metal lines used, and the estimated values of the velocity dispersions are given above the top panel in each figure. The velocity dispersion is the length of the radial velocity within which 90 percent of the cumulative optical depth is contained. The left and right vertical dashed lines in red are drawn corresponding to 5 percent and 95 percent of cumulative optical depth.

are essential to assess how common such Fe II blueshifts are.

5.2 Relative Abundances and Nucleosynthesis

Fig. 11 shows a plot of $[C/O]$ vs. $[O/H]$ for both the DLAs at $z \geq 4.5$ and the metal-poor DLAs at lower redshifts from the literature. Although the $z > 4.5$ DLAs are not always metal-poor, their average $[C/O]$ value of -0.19 ± 0.12

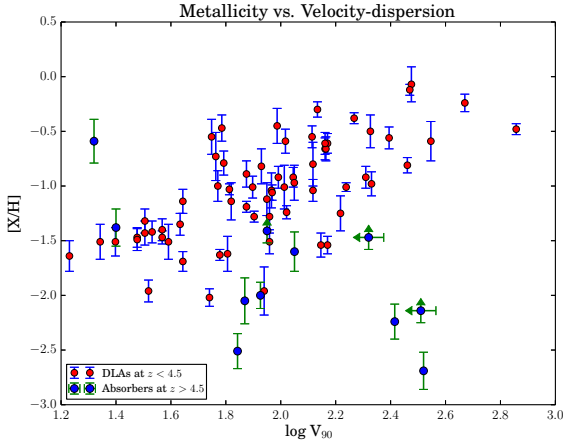


Figure 10. Plot showing metallicity vs. velocity-dispersion relation for volatile elements in DLA. Where X=O or S for $z \sim 5$ absorbers, and X=O, S or Zn for lower redshift DLAs. The red dots with blue error bars show the measurements for lower redshift DLAs from the literature. The blue dots with green error bars show the measurements for $z > 4.5$ absorbers taken from Poudel et al. (2018), Morrison et al. (2016), and this work. Lower and upper limits are represented by unidirectional arrows.

is consistent with that for the very metal-poor (VMP) DLAs, which have an average $[C/O]$ of -0.28 ± 0.12 (e.g. Cooke et al. 2011, 2017). Cooke et al. (2011, 2017) have suggested that metal-poor DLAs may have been enriched by metal-free progenitor stars. The similar $[C/O]$ ratios between metal-poor DLAs and the $z \sim 5$ DLAs suggest that DLAs at $z \sim 5$ may also have been enriched by early stars, including perhaps a leftover signature of Population III stars. Thus, it seems reasonable to compare the chemistry of metal-poor DLAs with the $z \sim 5$ DLAs to constrain the nature of the progenitor stars, especially their Initial Mass Function (IMF).

To this end, we have selected three $z \sim 5$ DLAs which have $[O/H] < -2.20$ (1 from this work and 2 from Poudel et al. (2018)) to compare with the nucleosynthesis models of massive metal-free stars from Heger & Woosley (2010). We compared $[C/O]$ in these 3 DLAs with those predicted by Heger & Woosley (2010), because $[C/O]$ is believed to put a strong constraint on the progenitor mass of Population III stars (e.g. Woosley & Weaver 1995; Heger & Woosley 2010; Cooke et al. 2011, 2017). The models of Heger & Woosley (2010) include 120 simulated stars spanning progenitor star masses in the range of 10-100 M_{\odot} , with a mass resolution of $\delta M > 0.1 M_{\odot}$. To consider the mixing between different stellar layers, these models use grids with 14 different mixing widths. Furthermore, the explosion energy of the supernova ranges from 0.3 to 10×10^{51} erg. The position of the piston just before the explosion is just below the oxygen burning shell where the entropy per baryon is given by $S/k_B = 4$, where k_B is the Boltzmann constant. We compared the $[C/O]$ and $[Si/O]$ ratios predicted by these various models with the ratios observed for our DLAs of interest, in order to estimate the range of progenitor mass, explosion energy, and mixing width that may have enriched

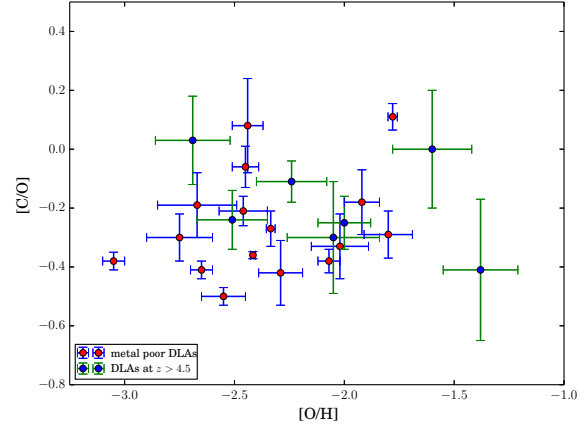


Figure 11. $[C/O]$ vs. $[O/H]$ for DLAs. The red dots with blue error bars show the measurements for metal-poor DLAs taken from Cooke et al. (2017). The blue dots with green error bars are the measurements for $z > 4.5$ absorbers which contain the measurements from Rafelski et al. (2012, 2014); Morrison et al. (2016); Poudel et al. (2018), and this work.

these DLAs. To accomplish this, we linearly interpolated this three-dimensional space and ran a Markov Chain Monte Carlo analysis using the techniques described in Cooke et al. (2017). The one- and two-dimensional projections of the samples are plotted in Fig. 12, 13 and 14 for the DLAs towards J0231-0728, J0306+1853 and J0824+1302 respectively. We were able to put a strong constraint on the progenitor masses for all of these DLAs. The probability distributions of the progenitor masses were centered around 14.6, 12.2, and 17.1 M_{\odot} for the $z = 5.335$, 4.987, and 4.809 DLAs towards J0231-0728, J0306+1853, and J0824+1302 respectively. The DLAs in the sight lines to J0231-0728 and J0824+1302 were taken from Poudel et al. (2018). The explosion energies were more or less constrained towards the upper end of the given range ($E_{\text{exp}} > 5 \times 10^{51}$ erg) for the DLAs towards J0306+1853 and J0824+1302 and $2-4 \times 10^{51}$ erg for the DLA towards J0231-0728. However, the mixing parameters could not be constrained well for any of our DLAs. Our results are roughly similar to those found by Cooke et al. (2017), who obtained a progenitor mass of 20.5 M_{\odot} and explosion energy of $6-8 \times 10^{51}$ erg for a VMP DLA at $z \approx 3.1$ with $[O/H]$ of -3.05.

5.3 Dust Depletion

To estimate the extent of depletion of elements on dust grains, Jenkins (2009) proposed a method using four parameters F_* , A_x , B_x , and Z_x . One of these parameters, F_* , manifests the strength of dust depletion for the given sight line. Higher value of F_* signifies higher depletion level. The other three parameters derived empirically by Jenkins (2009) are unique constants for each element X. They are related to the gas-phase abundance of element X and F_* by the relation $[X_{\text{gas}}/H] = B_x + A_x(F_* - Z_x)$. F_* , which represents the depletion strength for the given sight line, lies in range 0-1 for neutral gas in the Milky Way

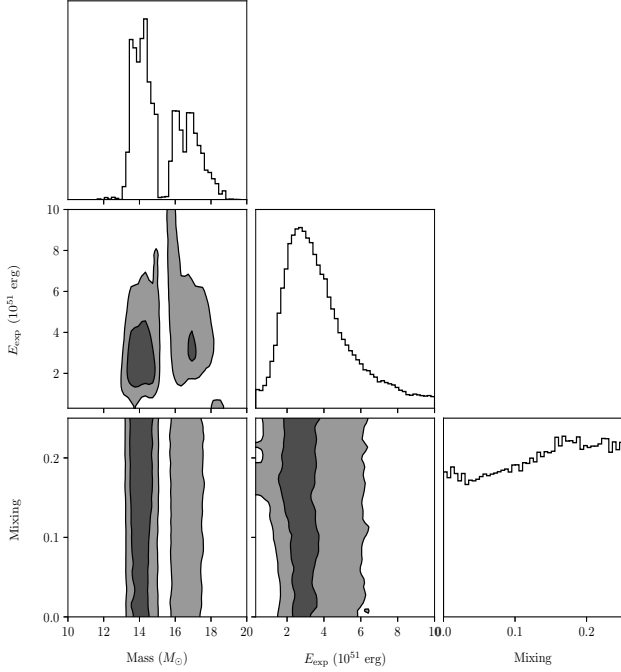


Figure 12. The one- and two-dimensional projections of the posterior probability distributions of progenitor mass, explosion energy, and the stellar mixing parameter of the star that might have enriched the DLA at $z = 5.335$ in the sight line to J0231-0728. We combined observed $[\text{C}/\text{O}]$ and $[\text{Si}/\text{O}]$ with the Heger & Woosley (2010) nucleosynthesis calculations, which comprised 16800 combinations of these three parameters. The marginalised probability of the model parameters on the x-axis are shown in the diagonal panel. The non-diagonal panels with dark and light shades are the two-dimensional projections of the parameters representing the 68 and 95 per cent confidence contours, respectively.

but is lower for warm-ionized gas (e.g. $F_* = -0.1$, Draine 2011). The values for A_x , B_x , and Z_x are presented in Jenkins (2009) and Jenkins & Wallerstein (2017). Jenkins & Wallerstein (2017) suggested that the values in the Small Magellanic Cloud (SMC) would be appropriate for studies of depletion in DLA and sub-DLA absorbers. In a plot of $[\text{X}/\text{H}]_{\text{obs}} - B_x + A_x Z_x$ vs. A_x , slope represents the F_* value and the intercept represents the depletion-corrected metallicity $[\text{X}/\text{H}]_{\text{intrinsic}}$ (see, e.g. Quiret et al. 2016).

Fig. 15 shows the plots of $[\text{X}/\text{H}]_{\text{obs}} - B_x + A_x Z_x$ vs. A_x to calculate the intrinsic metallicities and F_* values for four absorbers from this paper for which we have determinations of $[\text{O}/\text{H}]$ and the associated uncertainties (not just lower limits). We have adopted values of A_x , B_x , and Z_x for O and C from Jenkins (2009) and for Si, S, and Fe from Jenkins & Wallerstein (2017). The F_* values for these four absorbers are in the range from -0.81 ± 0.16 to -1.13 ± 0.19 . These values are closer to the MW's halo gas which shows $F_* = -0.28$ than the MW's cool disc gas, warm disc gas or disc + halo gas which have $F_* = 0.90, 0.12$, and -0.08 , respectively. Four other $z > 4.5$ absorbers in Poudel et al. (2018) and Morrison et al. (2016) showed F_* values comparable to

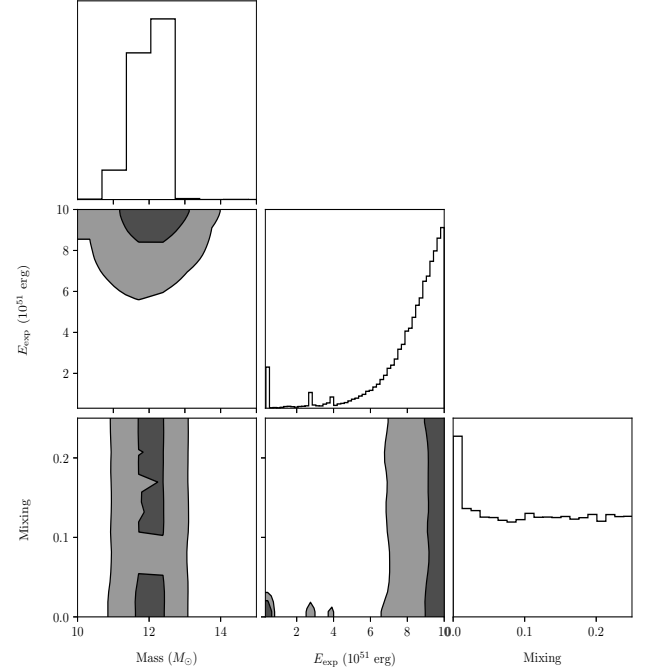


Figure 13. Same as Fig. 12 but for the DLA at $z=4.987$ in the sight line to J0306+1853.

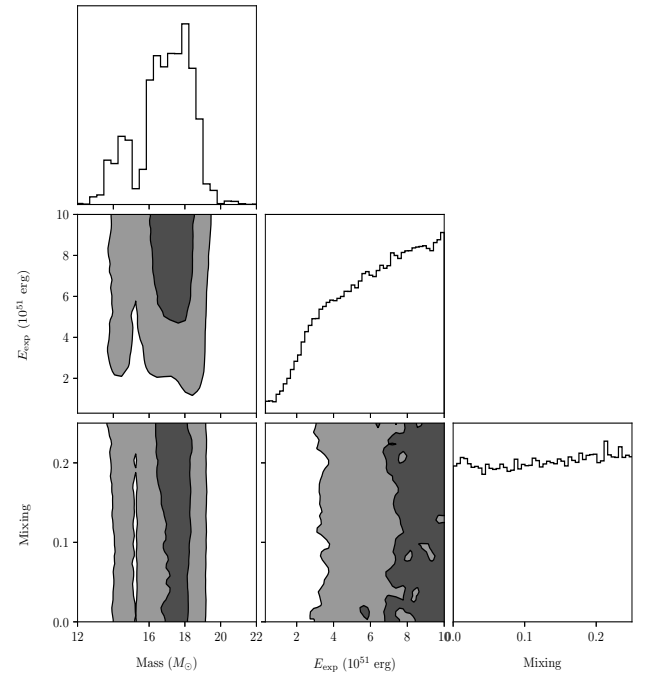


Figure 14. Same as Fig. 12 but for the DLA at $z=4.809$ in the sight line to J0824+1302.

those for the absorbers reported here. Overall, 5 of the 8 absorbers at $z > 4.5$ have F_* values equal to or greater than the typical value of -0.70 ± 0.06 found for lower-redshift DLAs by [Quiret et al. \(2016\)](#). Finally, the dust-corrected (i.e., intrinsic) metallicities obtained for these absorbers from Jenkins' approach are consistent with the observed $[O/H]$ values within the uncertainties. Furthermore, including the cases with limits, at least 3 out of 12 absorbers have $[Si/X] < 0$ and at least 4 out of 9 absorbers have $[Fe/X] < 0$, where X denotes O or S. Of the 8 systems with definitive measurements (not just limits) for $[Si/X]$, 2 show $[Si/X] < 0$ at $\gtrsim 2\sigma$ level. Of the 5 systems with definitive measurements (not just limits) for $[Fe/X]$, 2 show $[Fe/X] < 0$ at $\gtrsim 2\sigma$ level. While the samples are still small, it is clear that a significant fraction of $z > 4.5$ absorbers show depletions of Si and Fe. Thus, dust depletion appears to be significant in a substantial fraction of absorbers at $z > 4.5$.

5.4 Metallicity evolution

The cosmic mean metallicity of DLAs, also defined as the N_{HI} -weighted mean metallicity, $\langle Z \rangle$ is the ratio of the mean comoving densities of metals and hydrogen, given by $\langle Z \rangle = \log(\Omega_M/\Omega_H) - \log(M/H)_\odot$ where, Ω_M is the comoving density of metals and Ω_H is the comoving density of neutral hydrogen (e.g. [Lanzetta, Wolfe & Turnshek 1995](#); [Kulkarni & Fall 2002](#)). It is standard practice to use $\langle Z \rangle$ to investigate the metallicity evolution of DLAs (e.g. [Prochaska et al. 2003a](#); [Kulkarni et al. 2005, 2010](#); [Rafelski et al. 2012, 2014](#); [Som et al. 2015](#); [Quiret et al. 2016](#); [Poudel et al. 2018](#)). In this section, we determine the cosmic mean metallicity of DLAs at redshift $z > 4.5$ and compare it with previous measurement at $z > 4.5$ as well as $z < 4.5$.

The metallicity of DLAs decreases by ≈ 0.2 dex per unit increase in redshift as we go from $z = 0$ to $z = 4.5$ (e.g. [Prochaska et al. 2003a](#); [Kulkarni et al. 2005, 2007](#); [Som et al. 2013](#); [Rafelski et al. 2012](#); [Jorgenson et al. 2013](#); [Som et al. 2015](#); [Quiret et al. 2016](#)). At $z > 4.7$, a sudden decline of cosmic mean metallicity to a level of $\langle Z \rangle = -2.03$ (6σ below the prediction from lower-redshift DLAs) has been claimed (e.g. [Rafelski et al. 2012, 2014](#)). However, this conclusion was based on $z > 4.7$ measurements of primarily Si and Fe, which are refractory elements. Several studies have noted that such refractory elements are more strongly depleted on interstellar dust grains compared to volatile elements such as S, O, and Zn in the Milky Way interstellar medium (ISM) (e.g. [Savage & Sembach 1996](#); [Jenkins 2009](#)). Furthermore, a number of studies have noted the prevalence of dust depletion and the difference in depletions of refractory and volatile elements in DLAs (e.g. [Pettini et al. 1997](#); [Kulkarni, Fall & Truran 1997](#); [Jenkins 2009](#); [De Cia et al. 2016](#)). Indeed, several recent studies have noted that dust depletion exists in some DLAs even at $z \sim 5$ (e.g. [Morrison et al. 2016](#); [Poudel et al. 2018](#)). Therefore, to make a robust comparison between the metallicities of the absorbers at $z > 4.5$ and $z < 4.5$, we use the elements O, S, and Zn, which have lower condensation temperatures and thus lower depletion levels. The metallicity of DLAs based on O, S, and Zn is shown in Fig. 16.

As seen in Table 3 or in Fig. 16, for some of the

absorbers in our sample, we could only place lower limits on the metallicity. We include both these limits as well as the definitive determinations while calculating the mean metallicity $\langle Z \rangle$ using survival analysis, which allows estimation of the mean value and the associated error for measurements consisting of a mixture of detections and limits (either upper limits or lower limits). Each bin at $z < 4.5$ included 16 or 17 DLAs and the high-redshift bin (spanning $4.589 < z < 5.335$, with a median redshift of 4.83) included 14 absorbers with measurements of either O or S. The N_{HI} -weighted mean metallicity $\langle Z \rangle$ in the highest redshift bin (i.e. for $z > 4.5$) is -1.51 ± 0.18 , and is shown in Fig. 16 as a red pentagon. The binned N_{HI} -weighted mean metallicity of lower redshift systems is indicated as red circles with blue error bars and the corresponding linear best fit is shown as a solid blue line. The predicted metallicity from lower redshift data is consistent with our value in the highest redshift bin. The difference between the predicted and observed values is $< 0.5\sigma$, even if the uncertainty in the predicted value is ignored.

A few of the absorbers in our $z > 4.5$ sample are sub-DLAs (6 out of 14) rather than DLAs. It is interesting to ask whether the inclusion of these sub-DLAs is the cause of our cosmic mean metallicity being higher, given that sub-DLAs are found to be more metal-rich than DLAs at $z < 3$ (e.g. [Som et al. 2013, 2015](#); [Quiret et al. 2016](#)). We therefore repeated our calculations of the cosmic mean metallicity at $z > 4.5$ for only the DLAs, and found very little difference. The N_{HI} -weighted mean metallicity at $z > 4.5$ after excluding the sub-DLAs is -1.50 ± 0.16 . The negligible difference between the values obtained with and without the inclusion of sub-DLAs implies that either $\langle Z \rangle$ at $z > 4.5$ is dominated by absorbers with higher H I column densities, or that there is much less difference between the metallicity evolution trends for DLAs and sub-DLAs at these high redshifts. To help discriminate between these possibilities, we calculate the N_{HI} -weighted mean metallicity for just the sub-DLAs at $z > 4.5$, and find to be -1.36 ± 0.30 . Thus, it appears that the difference between the mean metallicities for DLAs and sub-DLAs is much smaller at $z > 4.5$ than at $z < 3$. This suggests that DLAs and sub-DLAs may have shared a common origin sometime during the second Gyr of cosmic history (i.e., sometime during $3 < z < 4.5$). However, observations of more DLAs and sub-DLAs at $z > 4.5$ are essential to understand how robust the results seen in the small existing samples are.

It thus appears that the cosmic mean metallicity at $4.6 \lesssim z \lesssim 5.3$ is consistent with the predictions based on the trend observed for DLAs at $z < 4.5$. This result differs from the conclusion of [Rafelski et al. \(2012, 2014\)](#) that there is a sudden drop in metallicity at $z > 4.7$. The difference may arise from our use of only the volatile elements S and O which have a lower condensation temperature and level of depletion in the MW ISM. This point has also been made by [Morrison et al. \(2016\)](#) and [De Cia et al. \(2018\)](#). Our result confirms the conclusion of [Poudel et al. \(2018\)](#) that the metallicity at $z > 4.5$ shows a smooth decrease rather than a sudden decline. Indeed, a gradual decrease agrees better with expectations than a sudden decline, in the absence of any evidence of a sudden change in the cosmic

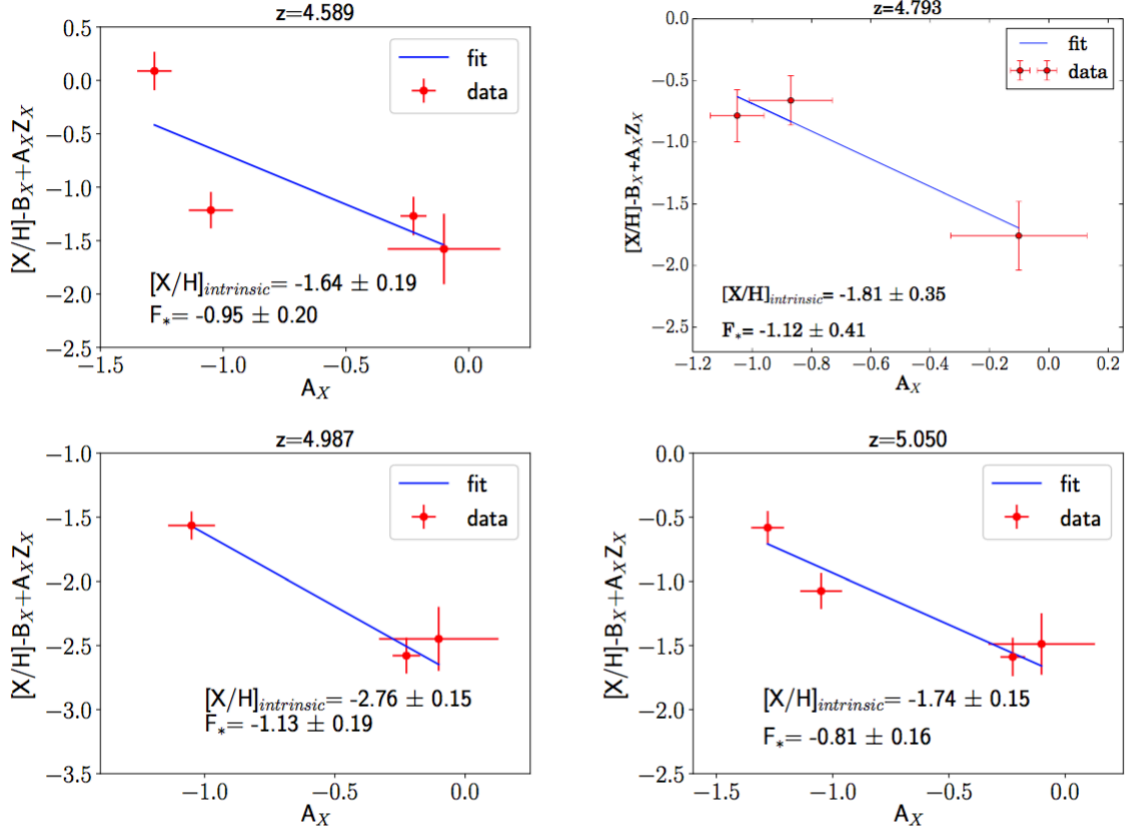


Figure 15. Plots showing $[X/H]_{obs} - B_X + A_X Z_X$ vs. A_X for four absorbers at $z = 4.589, 4.793, 4.987,$ and 5.050 . The F_* values and the depletion-corrected metallicity $[X/H]_{intrinsic}$ are shown in the bottom of each panel.

star formation history at or shortly before $z \sim 5$.

Furthermore, we note that the N_{HI} -weighted mean metallicity agrees within $\sim 1\sigma$ with the results from the n512RT64 simulation by Finlator et al. (2018), which predicts a value of -1.72 dex for the DLAs at $z = 5$.

Finally, as discussed in Section 2, we emphasize that these absorbers used to estimate the metallicity evolution were selected from the $z > 4.5$ SDSS absorbers listed in Noterdaeme et al. (2012) after checking that their SDSS spectra showed at least 1 metal line (regardless of its strength) at the same redshift as the H I line. The metal lines detected in the SDSS spectra were the lines with the highest oscillator strengths for the most abundant elements, i.e., O I λ 1302 and C II λ 1334. A non-detection of either of these lines was conservatively taken as an indication of non-reality of the system, given that identifications based on H I Lyman-alpha in SDSS data have been found to be unreliable for some absorbers (e.g. Crighion et al. 2015). We now assess the effect of the sample selection on the metallicity. To do this, we have determined the smallest metal column density that could be detected from the low-resolution and low-S/N SDSS data and the corresponding metal abundances for a typical N_{HI} value for our absorbers. To this end, we have performed simulations of O I λ 1302 and C II λ 1334 lines and measured their equivalent widths after convolving with the SDSS in-

strumental resolution to find the smallest column density that could be detected in the noisy SDSS spectra typical of the objects that were excluded from our sample. The selected quasar, J0807+1328 (RA: 08:07:15, Dec: +13:28:05.2) has an emission redshift of $z=4.876$ and the SDSS i-band magnitude of $m_i=19.39$. The absorber redshift ($z=4.678$) was reported by Noterdaeme et al. (2012) based on its Lyman-alpha measurements. This quasar has a S/N per pixel of ~ 14 near the redshifted O I λ 1302 line, which is comparable to the S/N per pixel of ~ 15 for our sample on average. These simulations show that the equivalent width of a hypothetical O I λ 1302 line for $\log N_{OI}=14.30$ would be 3 times the 1σ measurement uncertainty estimated from the S/N in the SDSS spectrum, i.e., $\log N_{OI}=14.30$ would have been detectable at a 3σ level (see Fig. 17). This limit of $\log N_{OI} = 14.30$ would correspond to a limiting metallicity of $[O/H]=-3.14$ dex and -2.79 dex, respectively, at the maximum and median H I column density values for our sample ($\log N_{HI} = 20.75$ and 20.40 , respectively). These limiting metallicity values are, respectively, > 42 times ($> 9\sigma$) and > 19 times ($> 7\sigma$) below the N_{HI} -weighted mean metallicity that we find for the systems that we do observe. Moreover, the limiting metallicity values of -3.14 and -2.79 dex are far below the N_{HI} -weighted mean of Rafelski et al. (2014; $-2.03^{+0.09}_{-0.11}$). Furthermore, the limit of $\log N_{CII} = 14.10$ which would be detected at 3σ level, corresponds to a limiting metallicity of $[C/H]=-3.08$ dex and -2.73 dex, respectively, at the maximum and me-

dian H I column density values for our sample. We show in Fig. 18 the detection significance of O I λ 1302 and C II λ 1334 lines for various column densities. The 3σ detection limit corresponds to $\log N_{\text{OI}} = 14.30$ and $\log N_{\text{CII}} = 14.10$, far below the column densities detected for our absorbers (see Table 2). Thus, the high mean metallicity we find is not a sample selection effect.

6 CONCLUSIONS

We have made seven new measurements of metal abundances at $z > 4.5$, doubling the existing sample for undepleted elements in gas-rich galaxies, and thus improving the constraints on the first ~ 1 billion years of cosmic metal evolution. Our main results are as follows:

1. We find a wide spread (factor of > 100) in the metallicities, which range from -2.69 dex to -0.59 dex. Our measurements include the highest metallicity observed in a sub-DLA at $z \sim 5$, with $[\text{S}/\text{H}] = -0.59 \pm 0.20$ for an absorber at $z = 4.793$ toward J1253+1046. In the same sight line, we also find a DLA at $z = 4.600$ with $[\text{O}/\text{H}] > -1.46$, which is the most metal-rich DLA known at $z \sim 5$.

2. Combining our sample with measurements from the literature, we examine the relative abundances in the $z \sim 5$ DLAs, and find their $[\text{C}/\text{O}]$ ratios to be consistent with those of the VMP DLAs. Furthermore, we estimate the probability distributions of the progenitor masses to be centered around $12 M_{\odot}$ to $17 M_{\odot}$, using $[\text{C}/\text{O}]$ and $[\text{Si}/\text{O}]$ for three relatively metal-poor $z \sim 5$ DLAs.

3. In a substantial fraction of absorbers at $z > 4.5$, the extent of dust depletion, as judged by the parameter F_* , appears to be at least as significant as (and in some cases stronger than) the typical depletion found in lower-redshift absorbers.

4. The metallicity vs. velocity dispersion relation for $z \sim 5$ absorbers seems to be different from that for lower redshift DLAs. The flatter trend observed for the $z \sim 5$ absorbers could be explained if these absorbers arise in galaxies with stronger inflows of chemically less enriched gas, or in more dark matter-dominated galaxies with smaller stellar masses.

5. We calculate the N_{HI} -weighted mean metallicity in the range $4.6 \lesssim z \lesssim 5.3$ and find it to be consistent with the prediction from lower redshifts DLAs, signifying a smooth decline in DLA metallicity rather than a sudden drop. Furthermore, we demonstrate that this high mean metallicity is not an artifact of sample selection.

6. The difference between the mean metallicities for DLAs and sub-DLAs at $z > 4.5$ is small, suggesting that DLAs and sub-DLAs may have been similar at this early epoch. The difference between the DLAs and sub-DLAs seen at $z < 3$ may have thus arisen sometime during $3 < z < 4.5$.

7. In 3 of the 4 absorbers where we have detected Fe II

absorption, the Fe II profile appears to be blue-shifted by $\sim 35 - 50 \text{ km s}^{-1}$ with respect to the O I, C II, and Si II profiles. Such a shift could be indicative of moderate-velocity outflows enriched in Fe II by type Ia supernovae. Alternately, the blue-shifted Fe II profiles may arise from stronger dust depletion of Fe II in the central components.

Our results demonstrate the value of obtaining high spectral resolution measurements of volatile elements such as O in absorbers at $z > 4.5$. Clearly, observations of more DLAs and sub-DLAs at $z > 4.5$ are essential to understand how robust the trends seen in the small existing samples are, and thus place more constraints on chemical enrichment of the gas in and around galaxies by early stars.

ACKNOWLEDGEMENTS:

We thank an anonymous referee for helpful comments that have improved this manuscript. SP, VPK, and FHC acknowledge partial support from NASA grants NNX14AG74G and NNX17AJ26G and NASA/STScI support for HST programs GO-12536, 13801 (PI Kulkarni). The authors would like to thank Dr. Xiaohui Fan for making his MagE data for J0306+1853 available to us after publication. The authors would also like to thank Dr. Ryan Cooke for providing his MCMC code to calculate progenitor star parameters from relative element abundances. CP thanks the Alexander von Humboldt Foundation for the granting of a Bessel Research Award held at MPA.

REFERENCES

- Abel T., Bryan G. L., Norman M. L., 2002, *Sci*, 295, 93
Aguirre A. et al. 2008, *ApJ*, 689, 851
Asplund M., Grevesse N., Sauval A. J., Jacques S. P. 2009, *ARA&A*, 47, 481
Becker G. D., Bolton J. S., Lidz A. 2015, *PASA*, 32, 45
Berg T. A. M. et al. 2019, *MNRAS*, 488, 3
Bromm V., Coppi P. S., Larson R. B., 1999, *ApJ*, 527, L5
Casey C. M., Narayanan D., Cooray A. 2014, *PhR*, 541, 45
Cashman F. H., Kulkarni V. P., Kisielius R., Ferland G. J., Bogdanovich P. 2017, *APJ*, 230, 8
Clark P. C., Glover S. C. O., Klessen R. S., Bromm V. 2011, *ApJ*, 727, 110
Cooke R., Pettini M., Steidel C. C., Rudie G., Nissen P. E. 2011, *MNRAS*, 417, 1534
Cooke R., Pettini M., Steidel C. C. 2017, *MNRAS*, 467, 802
Crighton N. H. M. et al. 2015, *MNRAS*, 452, 217
De Cia A., Ledoux C., Mattsson L., Petitjean P., Srianand R., Gavignaud I., Jenkins E. B. 2016 *A&A*, 596, 46
De Cia A., Ledoux C., Petitjean P., Savaglio S. 2018, *A&A*, 611A, 76
Dessauges-Zavadsky M., Peroux C., Kim T. S., D’Odorico S., McMahon R. G. 2003, *MNRAS*, 345, 447
Draine B. T. 2011, *EAS*, 46, 29
Erb D. K., Shapely A. E., Pettini M., Steidel C. C., Reddy N. A., Adelberger K. L., 2006, *ApJ*, 644, 813
Finlator K., Keating L., Oppenheimer B. D., Dave R., Zackrisson E. 2018, *MNRAS*, 480, 2628
Goldoni P. et al. 2006, Society of Photo-Optical Instrumentation Engineers (SPIE) Conference Series, 6269, 62692
Gonzalez V. et al. 2011, *ApJ*, 735L, 34

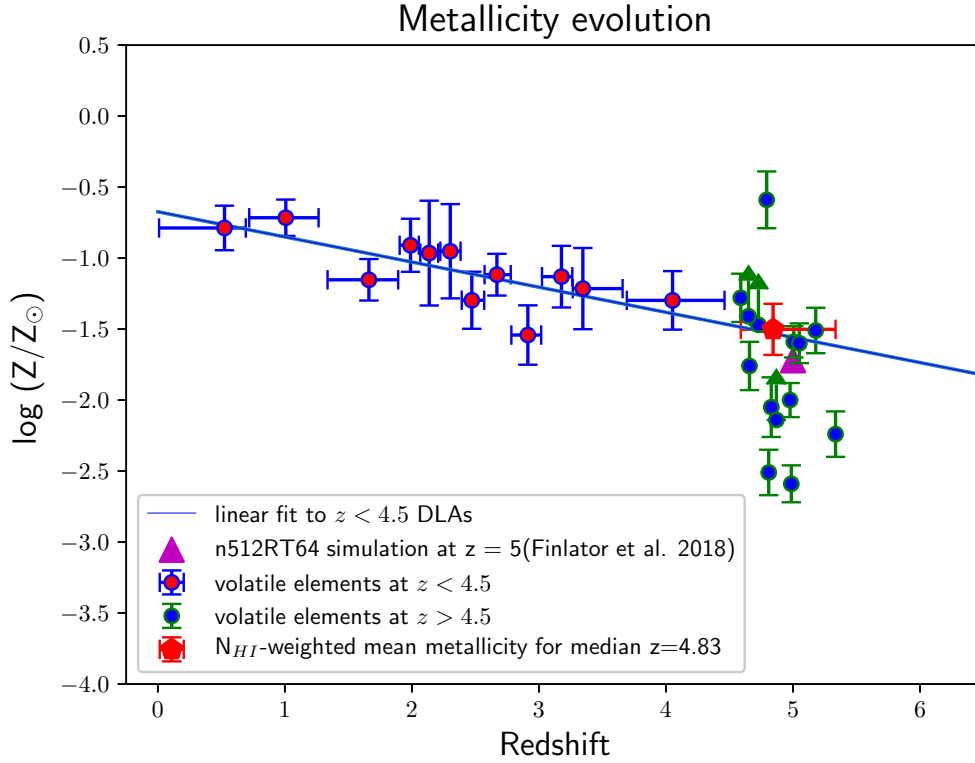


Figure 16. Metallicity evolution with redshift. The red dots with blue error bars are the binned N_{HI} -weighted mean metallicities of DLAs at $z < 4.5$ using volatile elements from the literature, with each bin containing 16 or 17 DLAs and the solid blue line showing the corresponding best fit. The blue dots with green error bars are the individual measurements for $z > 4.5$ absorbers also using volatile elements. Three of these measurements are taken from Rafelski et al. (2012, 2014), one from Morrison et al. (2016), three from Poudel et al. (2018), and seven from this paper. The N_{HI} -weighted mean metallicity at a median redshift of $z = 4.83$ for all absorbers in the $z > 4.5$ bin is shown by a pentagon in red. The binned means and the corresponding errors are calculated using survival analysis to handle a mixture of detections and limits. For comparison, the N_{HI} -weighted mean metallicity of DLAs at $z = 5$ for the n512RT64 simulation from Finlator et al. (2018) is shown by a triangle in magenta.

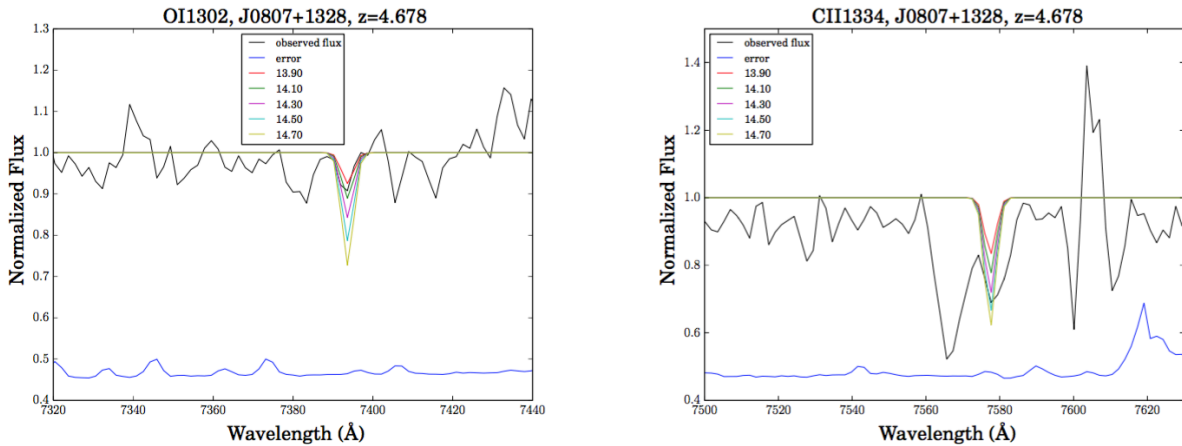


Figure 17. Overplotting of different column density ($\log N_{\text{OI}}$ and $\log N_{\text{CII}}$) profiles convolved with SDSS resolution using typical SDSS spectra excluded from our sample to determine the SDSS metallicity floor. In each case, the observed continuum normalized flux is shown in black and the the 1σ error in the normalized flux is shown in blue at the bottom of each panel and is shifted by $+0.4$ for the purpose of displaying on the same scale. The metal line, sightline to the quasar, and redshift are given at the top of the figures in each panel.

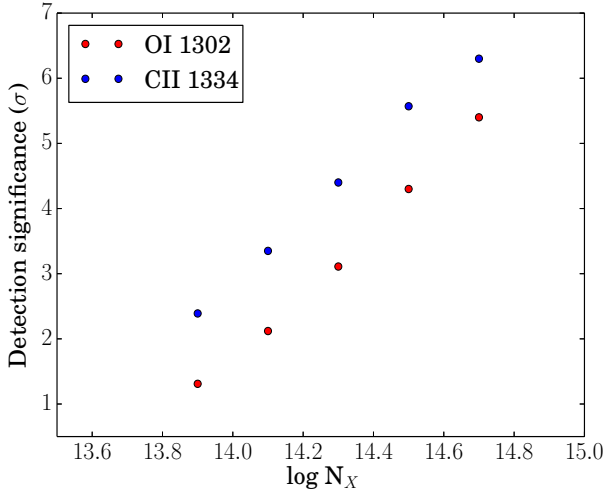


Figure 18. Detection significance of O I λ 1302 and C II λ 1334 in the SDSS spectrum of J0807+1328 for different column densities for a hypothetical intervening absorber at $z=4.678$.

Heger A. & Woosley S. E. 2010, ApJ, 724, 341
 Hirano S., Hosokawa T., Yoshida N., Umeda H., Omukai K., Chiaki G., Yorke H. W., 2014, ApJ, 781, 60
 Jenkins E. B. 2009, ApJ, 700, 1299
 Jenkins E. B. & Wallerstein G. 2017, ApJ, 838, 19
 Jorgenson R. A., Murphy M. T., Thompson R. 2013, MNRAS, 435, 482
 Kulkarni G., Rollinde E., Hennawi, Joseph F., Vangioni, E. 2013, ApJ, 772, 93
 Kulkarni V. P. & Fall S. M. 2002, ApJ, 580, 732
 Kulkarni, V. P., Fall S. M., Truran J. W. 1997, ApJ, 484L, 7
 Kulkarni V. P., Fall S. M., Lauroesch J. T., York D. G., Welty D. E., Khare P., Truran J. W., 2005, ApJ, 618, 68
 Kulkarni V. P., Khare P., Péroux C., York D. G., Lauroesch J. T., Meiring J. D., 2007, ApJ, 661, 88
 Kulkarni V. P., Khare P., Som D., Meiring J., York D. G., Péroux C., Lauroesch J. T. 2010, NewA, 15, 735
 Kulkarni V. P., Som D., Morrison S., Péroux C., Quiret S., York D. G. 2015, APJ, 815, 24
 Lanzetta K. M., Wolfe A. M., Turnshek D. A. 1995, ApJ, 440, 435
 Ledoux C., Petitjean P., Moller P., Fynbo J., Srianand R., 2006, A&A, 457, 71
 Lehner N., 2013, ApJ, 770, 138
 Madau P. & Dickinson M. 2014, ARA&A, 52, 415
 Maio U. & Tesconi E. 2015, MNRAS, 453, 3798
 Meiring J. D., Lauroesch J. T., Kulkarni V. P., et al. 2009, MNRAS, 397, 2037
 Moller P., Fynbo J. P. U., Ledoux C., Nilsson K. K. 2013, MNRAS, 430, 2680
 Morrison S., Kulkarni V. P., Som D., DeMarcy B., Quiret S., Péroux C. 2016, ApJ, 830, 13
 Morton D. C., 2004, ApJS, 151, 403
 Nagamine, K., Springel, V., Hernquist, L. 2004, MNRAS, 348, 421
 Nagamine, K.; Springel, V.; Hernquist, L. 2004, MNRAS, 348, 385
 Nakamura F. & Umemura M., 2001, ApJ, 548, 19
 Noterdaeme P. et al. 2012, A&A, 547, L1
 Penprase B. E., Prochaska J. X., Sargent Wallace L. W., Tor-Martinez I., Beeler D. J. 2010, ApJ, 721, 1
 Pettini M. et al. 1994, ApJ, 426, 79

Pettini M., King D. L., Smith L. J., Hunstead R. W. 1997, ApJ, 478, 536
 Péroux C., Dessauges-Zavadsky M., D’Odorico S., Kim T.-S., McMahon R. G. 2003, MNRAS, 345, 480
 Poudel S., Kulkarni V. P., Morrison S., Péroux C., Som D., Rahmani H., Quiret S. 2018, MNRAS, 473, 3559
 Prochaska J. X., Gawiser E., Wolfe A. M., Castro S., Djorgovski S. G. 2003a, ApJ, 595, L9
 Prochaska J. X., Gawiser E., Wolfe A. M., Cooke J., Gelino D. 2003b, ApJ, 147, 227
 Quiret S. et al. 2016, MNRAS, 458, 4074
 Rafelski M., Wolfe A. M., Prochaska J. X., Neeleman M., Mendez A. J., 2012, ApJ, 755, 89
 Rafelski M., Neeleman M., Fumagalli M., Wolfe A. M., Prochaska J. X. 2014, ApJ, 782, L29
 Rahmani H. et al. 2016, MNRAS, 463, 980
 Savage B. D., & Sembach K. R. 1991, ApJ, 379, 245
 Savage B. D., & Sembach K. R. 1996, ARAA, 34, 279
 Som D., Kulkarni V. P., Meiring J., York D. G., Péroux C., Khare P., Lauroesch J. T. 2013, MNRAS, 435, 1469
 Som D. et al. 2015, ApJ, 806, 25
 Stacy A. & Bromm V., 2013, MNRAS, 433, 1094
 Stacy A., Bromm V., Lee A. T., 2016, MNRAS, 462, 1307
 Wang F. et al. 2015, ApJ, 807L, 9
 Wolfe A. M., Gawiser E., Prochaska J. X., 2005, ARA&A, 43, 861
 Wolfe A. M., Chen H. 2006, ApJ, 652, 981
 Wolfe A. M., Prochaska J. X., 1998, ApJ, 494, 15
 Woosley S. E. & Weaver T. A. 1995, ApJS, 101, 181
 Zafar T., Péroux C., Popping A., Milliard B., Deharveng J. M., Frank S. 2013, A&A, 556, 141

APPENDIX A: ASSESSMENT OF METAL LINE SATURATION

Here we discuss the estimates of the limits on O I and C II column densities in cases where the lines are strong. Fig. A1 shows overplotting of different column density ($\log N_X$, where, $X=OI$ or CII) profiles to estimate the extent of saturation.

APPENDIX B: VELOCITY PLOTS FOR LYMAN-SERIES LINES

Examples of velocity plots of Lyman-series lines for our systems are shown below. It is clear from these plots that in these cases, Lyman lines beyond Lyman-alpha are not useful for estimation of H I column densities.

This paper has been typeset from a $\text{\TeX}/\text{\LaTeX}$ file prepared by the author.

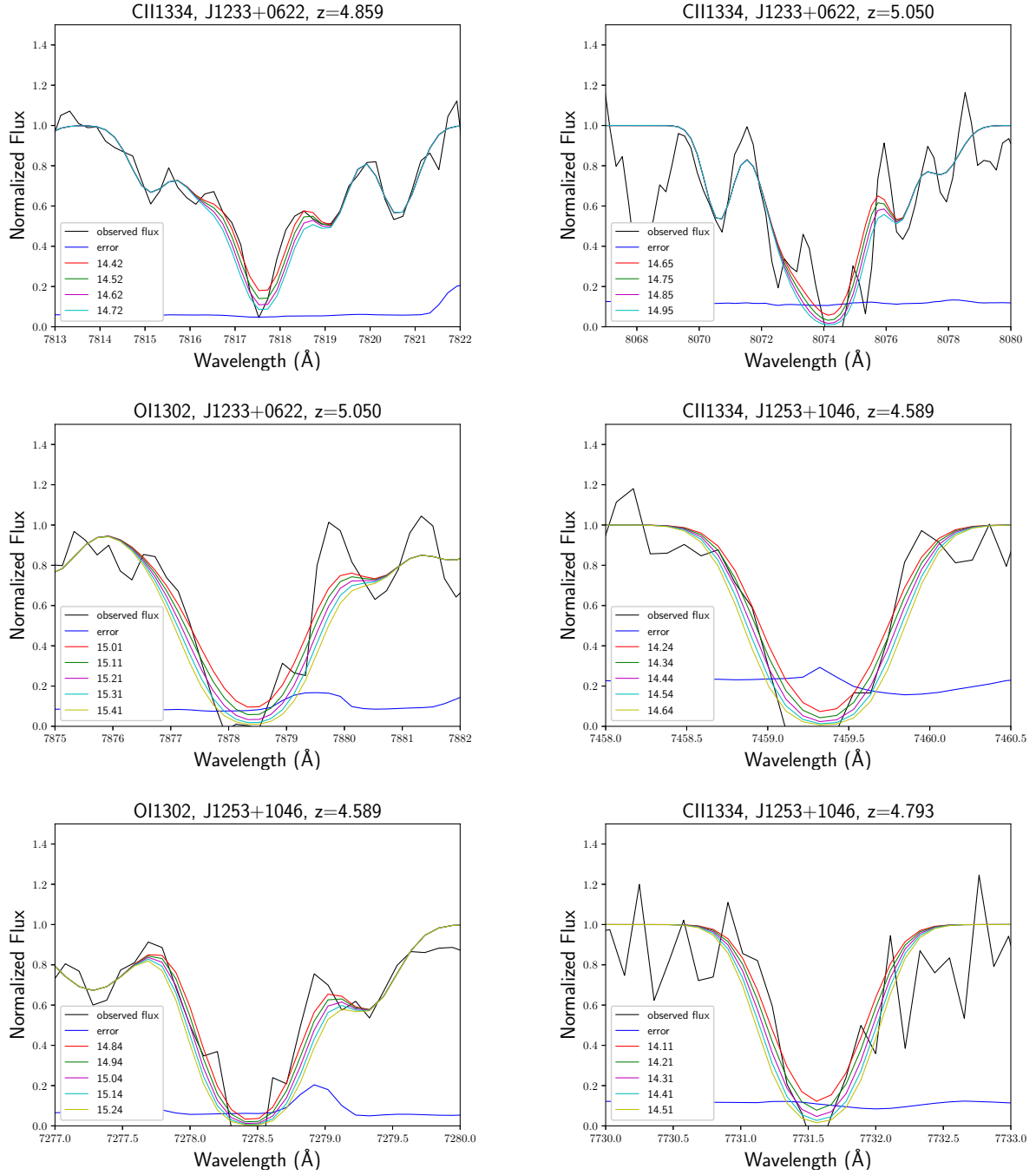


Figure A1. Overplotting of different column density ($\log N_X$, where, $X=OI$ or CII) profiles to estimate the extent of saturation. In each case, the observed continuum normalized flux is shown in black and the 1σ error in the normalized flux is shown in blue at the bottom of each panel. The metal line, sightline to the quasar, and redshift are given at the top of the figures in each panel.

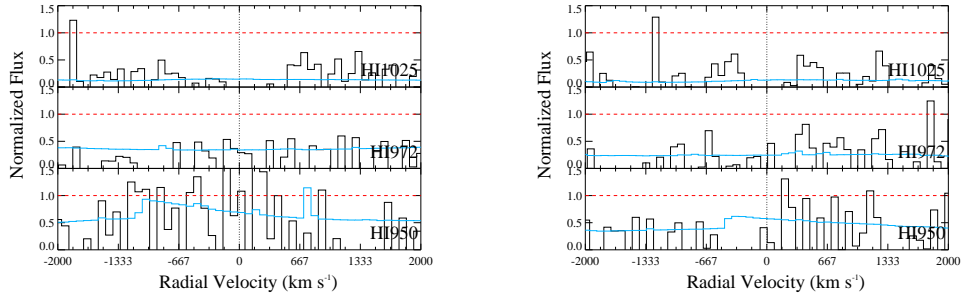


Figure B1. Velocity plots for Lyman-beta, Lyman-gamma, and Lyman-delta for the absorbers at $z=4.859$ (Left) and $z=5.050$ (Right) towards J1233+0622. The corresponding Lyman-alpha lines are shown in Fig. 1. In each panel, the vertical dotted line is at the center of the Lyman-alpha line of the corresponding absorber, the continuum level is shown by horizontal dashed line in red, the observed data are shown in black, and the blue line at the bottom shows the 1σ error in the normalized flux.

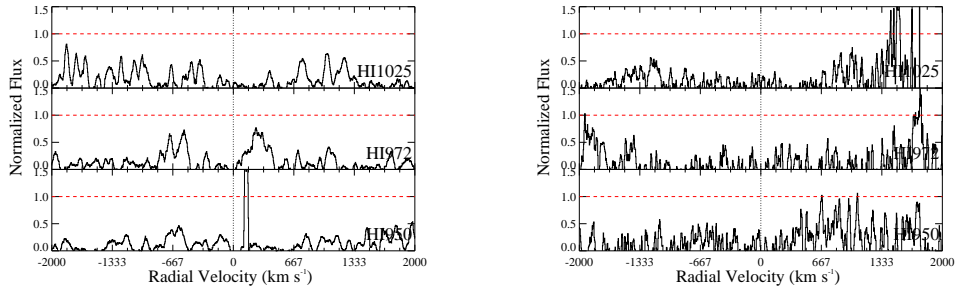


Figure B2. Velocity plots for Lyman-beta, Lyman-gamma, and Lyman-delta for the absorbers at $z=4.793$ (Left) and $z=4.627$ (Right) towards J1253+1046 and J1557+1018 respectively. In each panel, the vertical dotted line is at the center of the Lyman-alpha line of the corresponding absorber, the continuum level is shown by horizontal dashed line in red, the observed data are shown in black.